NAG 3-2695

Unsteady Aerodynamic Response of a Linear Cascade of Airfoils in Separated Flow

Vincent R. Capece Christopher Ford Christopher Bone
Rui Li

September 30, 2004

Abstract

The overall objective of this research program was to investigate methods to modify the leading edge separation region, which could lead to an improvement in aeroelastic stability of advanced airfoil designs. The airfoil section used is representative of current low aspect ratio fan blade tip sections. The experimental potion of this study investigated separated zone boundary layer □ow removal through suction slots. Suction applied to a cavity in the vicinity of the separation onset point was found to be the most effective location. The computational study looked into the in□uence of front camber on □utter stability. To assess the in□uence of the change in airfoil shape on stability the work-per-cycle was evaluated for torsion mode oscillations. It was shown that the front camberline shape can be an important factor for stabilizing the predicted work-per-cycle and reducing the predicted extent of the separation zone.

In addition, data analysis procedures are discussed for reducing data acquired in experiments that involve periodic unsteady data. This work was conducted in support of experiments being conducted in the NASA Glenn Research Center Transonic Flutter Cascade. The spectral block averaging method is presented. This method is shown to be able to account for variations in airfoil oscillation frequency that can occur in experiments that force oscillate the airfoils to simulate □utter.

CONTENTS

List of Figures

List of Tables

1. INTRODUCTION

1.1. Background

One of the challenges in the design and development of fan and compressor blades for aircraft gas turbine engines is □utter. Flutter, in general, produces large vibration stress and limits the life of turbomachine blades. To increase the efficiency of fans and compressors and reduce weight, current design trends are for thinner blades with increased loading per blade. These design practices produce blade designs that are more susceptible to □utter. When a blade encounters □utter it results in an extensive redesign program. During this redesign process the desired aerodynamic shape is altered to eliminate □utter from the engine operating regime. The resulting blade design often generates lower stage efficiency, and in many instances increased engine weight.

There are many different types of □utter that can occur in fans and compressors; Figure 1.1 illustrates the □utter regions on a compressor performance map. Subsonic/transonic stall □utter, schematically depicted near the stall line at part speed, is the most difficult type of □utter to predict accurately because viscous effects are signi□cant. For these types of □ows the Navier-Stokes equations need to be used. The unsteady Reynolds Averaged Navier-Stokes equations have been developed to account for viscous effects (e.g., Chen, J. P., and W. R. Briley[1], Weber and Platzer[2], Swafford et al.[3], Ekaterinaris and Platzer[4], Sidén[5], and Wu et al.[6]). For these Reynolds averaged equations turbulence models are needed for the Reynolds stress terms. A transition model is also necessary, but in most cases the transition location is speci□ed at the leading edge. Since the Reynolds numbers in turbomachinery are large enough to guarantee the □ow is turbulent, suitable transition and turbulence models are crucial for accurate prediction of steady and unsteady separated □ow.

Due to the mathematical assumptions, experimental data are needed to verify these models and to indicate necessary re□nements. Unfortunately, only a limited quantity of unsteady aerodynamic data exists at large mean incidence angles (e.g.

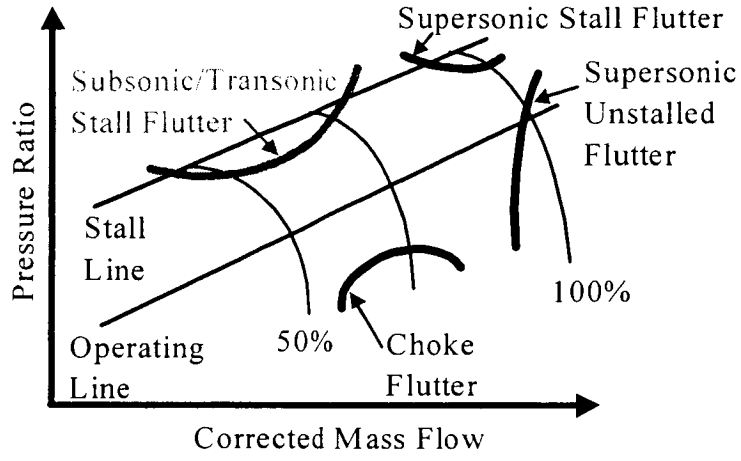

Figure 1.1: Compressor performance map showing flutter boundaries.

Carta and St. Hilaire[7], Carta and St. Hilaire[8], Carta[9], Buffum et. al.[10] and Buffum et. al.[11]). In fact, the significant effects of unsteady separated flow at realistic reduced frequencies and Mach number values have not been completely addressed.

1.2. Objectives

The goals of this research program were to investigate two methods that could potentially be used for flutter control when flow separation is present. These methods are flow control type methods. The first is flow control through boundary layer suction and the second is flow control through airfoil shape modifications in the leading edge region.

The specific research objectives are listed below:

1. Modify the University of Kentucky, Paducah (UKP) wind tunnel test section to allow testing of a cascade modeled after the NASA Glenn Research Center Transonic Flutter Cascade.

2. Design an airfoil for the UKP wind tunnel with suction slots for separation flow control.

3. Perform preliminary testing of the cascade airfoils with □ow control in the new test cascade test section.

4. Investigate the in□uence of airfoil morphing on □utter stability.

In addition, in support of the work that was being conduction in the NASA GRC TFC, research was conducted on signal processing of periodic □ow measurements and correction of blade mounted pressure transducer signals for oscillation effects.

2. TECHNICAL APPROACH

The approach used to achieve the objectives listed above involves performing experiments in the University of Kentucky, Paducah (UKP) wind tunnel and computational modeling. The research was conducted using a modern airfoil cross-section.

2.1. Airfoil Design

The airfoils used in this study have a cross-section similar to that found in the tip region of current low aspect ratio fan blades. The airfoil section was designed using the Pratt & Whitney (P&W) fan and compressor aerodynamic design system, which is for □ow in circular ducts. To simulate the □ow in the linear cascade, the airfoils were designed using a radius ratio of 0.99. The loading levels, losses, solidity, and stagger angle are consistent with modern design practice for fan blades. The airfoil cascade parameters are given in Table 2.1, and Figure 2.1 illustrates the geometry de□nitions.

Table 2.1: Airfoil and cascade parameters

Chord, C	89.2 mm
Maximum thickness, t_{max}	0.048 C
Location of maximum thickness, x_{max}	0.625 C
Camber angle, θ^*	-9.5°
Number of airfoils	9
Stagger angle, Θ	60°
Solidity, C/S	1.52
Pitching axis, (x_{pitch}/C, y_{pitch}/C)	(0.5, -0.017)

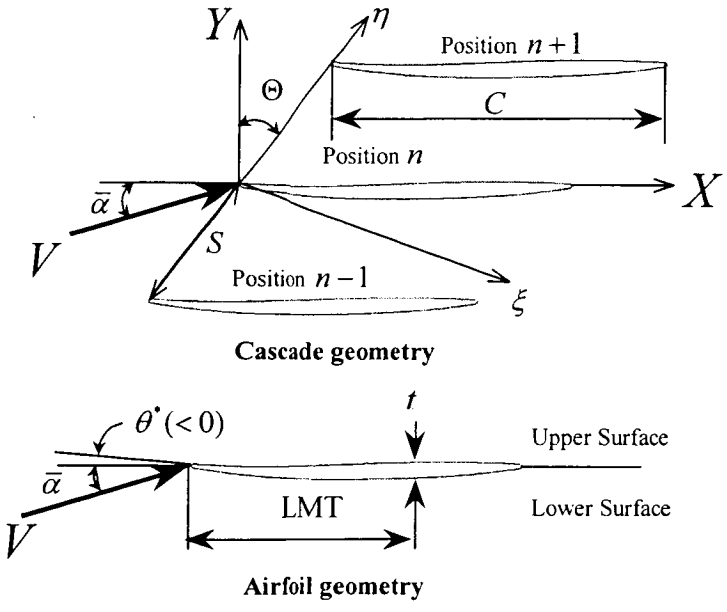

Figure 2.1: Airfoil and cascade geometry.

3. Experimental Investigation

A series of experiments were conducted in the UKP Wind Tunnel. These experiments concentrated on methods to modify the leading edge separated □ow region. The interest in boundary layer separation control has a rich history with many contributors. Recently there has been renewed interest in this area, which has been largely driven by the miniaturization of electromechanical devices. Hence, some of the more recent literature, which is applicable to this research program, will be discussed. The references in these papers can be consulted for additional background information.

Yoshihara and Zonars[12] investigated the in□uence of a jet of □uid directed downward near the trailing edge of an airfoil □ap ('jet-□ap') on the lift and drag of a transonic airfoil. The results of this study indicated that this device was able to increase lift. Seifert et al.[13] used oscillatory blowing to delay separation on a □apped NACA 0015 airfoil. The chordal Reynolds numbers in this experiment ranged from 0.1 to 1 *Million*. The wall jet originated from a slot located above the hinge of the □ap. The □ap length was 25% of the airfoil chord. Flap de□ections of 20° and 40° were used. Using small amounts of steady blowing with a relatively low amount of □ow oscillation resulted in signi□cant increases in the lift at all incidence angles investigated.

This later work was extended by Seifert, et al.[14] to include different airfoil geometries that included a NACA 0015 airfoil with a leading edge slot and an oscillating □ap located near the leading edge. The maximum chordal Reynolds number in this investigation was 1.2 *Million*. Results indicated that the employment of periodic oscillations in turbulent boundary layers permits larger pressure gradients without separation. This increases the lift at angles-of-attack and □ap de□ections where the boundary layer would normally be separated. To control separation it was found that the oscillations introduced into the □ow should become a maximum in the vicinity of the separation point. Hence, the most efficient location of an actuator is near the separation location.

Seifert and Pack [15] performed further experiments with a NACA 0015 air-

foil using the NASA Langley Research Center 0.3-m Transonic Cryogenic Wind Tunnel. In this investigation the chordal Reynolds number ranged from 8 to 28.2 *Million* for most experiments. Active control of the boundary layer separation was demonstrated at these Reynolds numbers using oscillatory excitation as was done in previous investigations.

Closed-loop digital feedback control was implemented on a model of a 20% thick airfoil that was a variation of the Glauert Glas II airfoil by Allan et al.[16]. This thick airfoil had a favorable pressure gradient up to 55% chord followed by a severe adverse pressure gradient that generated separation in the 66% chord region. The chordal Reynolds number in these experiments was 16 *Million*. Employing oscillatory □ow excitation just upstream of the separation point reduced boundary layer separation. The amplitude of the oscillatory excitation controlled the reduction in the separation region.

This model was also used by Seifert and Pack[17] to conduct a series of experiments at chordal Reynolds numbers from 2 to 40 *Million* using □ow oscillation as well as steady blowing or steady suction. Steady blowing or suction was able to fully reattach the □ow and recover the ideal pressure distribution. Furthermore, weak suction with a superimposed periodic excitation was found to increase the sensitivity of the shear layer to oscillation frequency.

The concept of using boundary layer suction for fan and compressor blades is being investigated to generate higher pressure ratios per stage (Kerrebrock et al.[18] and Kerrebrock et al.[19]). This approach is interesting in that it would decrease the number of stages in a fan or compressor, which would reduce engine weight. Furthermore, the separation control used by this method has the potential to control the stall □utter response of fan and compressor blades.

At 10° chordal incidence angle the airfoils used in this investigation separate in the vicinity of the leading edge circle on the suction surface with a reattachment point in the 46% chord region for a Mach number of 0.5.

3.1. Wind Tunnel Modi□cations

The University of Kentucky, Paducah (UKP) wind tunnel, which is schematically depicted in Figure 3.1, draws air from the atmosphere through a set of screens into a 20.6:1 smoothly contracting inlet. The contracting inlet exits into a rectangular test section; the frames for the test section and inlet are on casters with leveling screws to permit rapid disassembly of the tunnel to interchange test sections. The test section exits into a slowly diverging duct that transitions from a rectangular

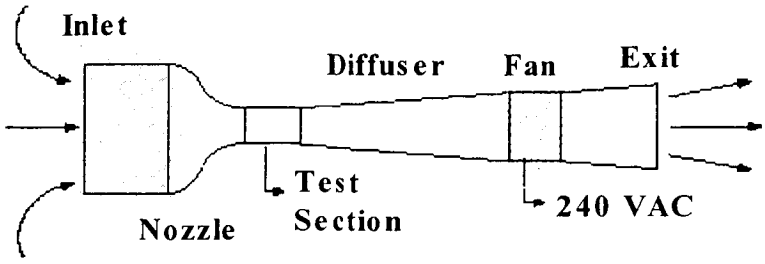

Figure 3.1: Schematic of UKP wind tunnel.

cross-section into a circular cross-section for the fan assembly. A 50 HP motor drives the fan. Downstream of the fan assembly, the □ow exhausts to atmosphere after passing through an exit diffuser.

The traditional wind tunnel test section was replaced with a cascade test section. The new cascade test section was modeled after the test section of the NASA Glenn Research Center Transonic Flutter Cascade (TFC)[10][20][21], see Figure 3.2. The converging inlet section is connected to a transition duct. The walls of the transition duct are set to provide a 10° chordal incidence angle to the NASA/P&W airfoil. The exit side walls are set at a 24° angle[20],[21] and the □ow exits into the diffuser portion of the wind tunnel. Additionally, the top wall is made of Plexiglas to provide optical access to the test section. The test section was constructed to hold nine airfoils that have a chord length of 13 *in.* (330.2 *mm*). The solidity and blade geometry are the same as those used in the TFC. The size of the inlet and diffuser of the existing tunnel and limitations of the rapid prototyping (stereo lithography) machine used to produce the airfoils restricted the chord length of the airfoils. The chordal Reynolds number for this chord length is approximately 1 *Million.* This is similar to the chordal Reynolds number in the TFC.

Regular pneumatic taps in the walls of the tunnel were used to measure the inlet and exit static pressures. These measurements were used to determine the cascade pressure rise, inlet Mach number, inlet static density, and inlet static temperature. A cobra probe used upstream of the airfoils measured the stagnation pressure and □ow angularity. Airfoils instrumented with static pressure taps were used to quantify the steady aerodynamic loading.

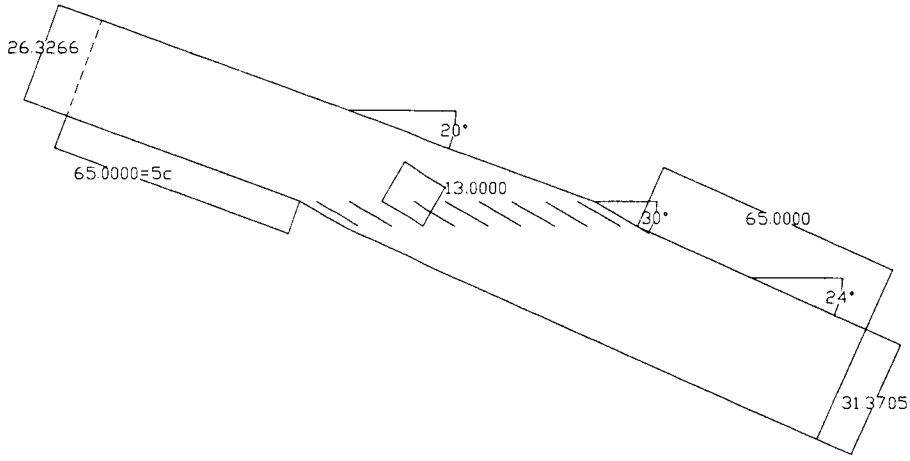

Figure 3.2: Schematic diagram of UKP nine airfoil cascade test section.

3.2. Airfoil Flow Control Design

The airfoil contour used in this investigation was the NASA/P&W airfoil, which was previously presented in Section 2.1. The cascade airfoils were made at the University of Kentucky Center for Manufacturing by a rapid prototyping (stereo lithography) machine. The material is SOMOS 7SLA, which is a sand-able plastic-type material. The rapid prototyping machine is limited to a blade chord of 13 *in.* (330.2 *mm*) and the tunnel required the span of the blade to be 20.5 *in.* (520.7 *mm*). The rapid prototyping machine's maximum building capability is 13x10x10 *in.* (330.2x254x254 *mm*). Due to this fact, the blades were made in two pieces and mated together at approximately 73% span to arrive at the required 20.5 *in.* (520.7 *mm*) span length.

Conventional surface static pressure taps were integrated into the blade design. The location of the pressure taps were chosen to allow greater resolution of the surface pressure on the airfoil near the leading and trailing edges, as illustrated in Figure 3.3. Pressure taps are also located at 5%, 25%, and 95% span.

Cavities with slots that extend to the suction surface of the blade were also integrated into the airfoils, which were used to control the separated boundary layer. Three separate designs were fabricated as illustrated in Figure 3.4 (Con□guration

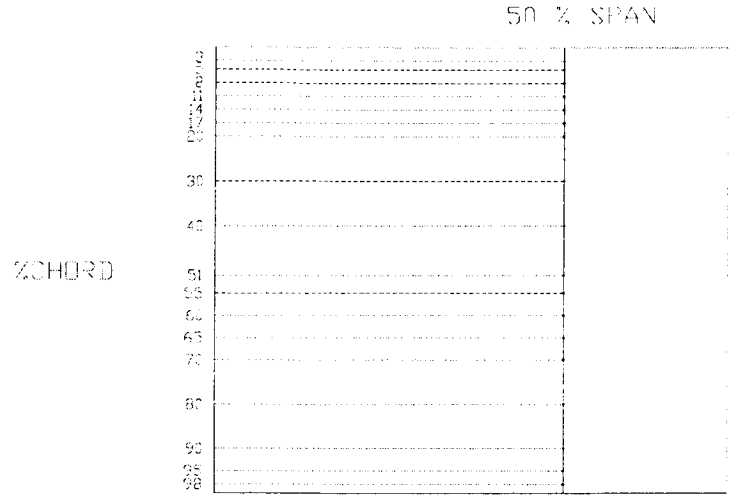

Figure 3.3: Schematic of midspan airfoil surface steady pressure measurement locations.

1), Figure 3.5 (Con□guration 2), Figure 3.6 (Con□guration 3). The slots extended over the entire span of the airfoil and were placed based on the □ow visualization test conducted in the TFC and computational simulations using **TURBO**[1] and **NPHASE**[3],[22]. The slot nearest the leading edge for all three con□gurations was placed just downstream of the leading edge circle, because the □ow over this airfoil at 10° chordal incidence separates immediately after the leading edge circle, and it is desirable to have the boundary layer control slot near the separation onset point. The slot farthest from the leading edge for slot con□gurations 1 and 3 were placed near the mid-chord where TFC experiments showed the boundary layer reattached. The middle slot location for slot con□gurations 1 and 3 was positioned in the area expected to have the thickest region of separated □ow based on computational simulations. The slot con□guration 2 airfoil has a leading edge slot that is angled upstream rather than downstream as the other slots to investigate the effects of suction entrance orientation. This airfoil also features a second slot farther from the leading edge, but closer than the comparable slots from the other con□guration to further investigate the effect of slot entrance orientation on separated □ow control. The 0.25% chord width of the boundary layer control slots is based on similar slots used by Seifert and Pack[17]. The primary □ow control

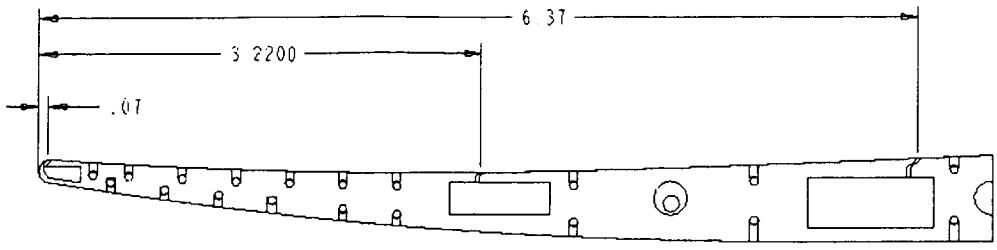

Figure 3.4: Boundary layer control cavity configuration 1.

mechanism will be boundary layer suction. However, boundary layer blowing could also be utilized. Boundary layer suction was accomplished using vacuum type pumps.

Figure 3.7 shows a photograph of two of the cavities for configuration 1 along the airfoil split line. The mid and aft cavities are clearly visible along with the alignment pins. The static pressure taps are also visible. Stainless steel tubing was used in the static tap holes to insure leak free connections between the two airfoil sections. Furthermore, RTV was used when joining the two sections together to prevent leaks from the cavities or static tapping at the split line.

3.3. Results

Testing has been performed and is continuing on cavity configuration 1, which will be discussed below. The test section inlet Mach number was 0.12 and the Reynolds number based on airfoil chord was approximately 1 *Million*.

The steady surface pressure coefficient $\left(C_p = \frac{P_{in}-P}{\rho_{in}V_{in}^2}\right)$ is presented in Figure 3.8 for the case when no suction is present. The no flow control data exhibits a plateau in the pressure coefficient distribution on the suction surface up to approximately 20% chord. This is characteristic of separated flow that originates in the leading edge region. Downstream of this region there is a rapid drop in the pressure coefficient as the flow approaches the covered section of the flow passage.

Various combinations of suction applied to the three cavities for configuration 1 were investigated. In all cases suction was applied to only the center airfoil in

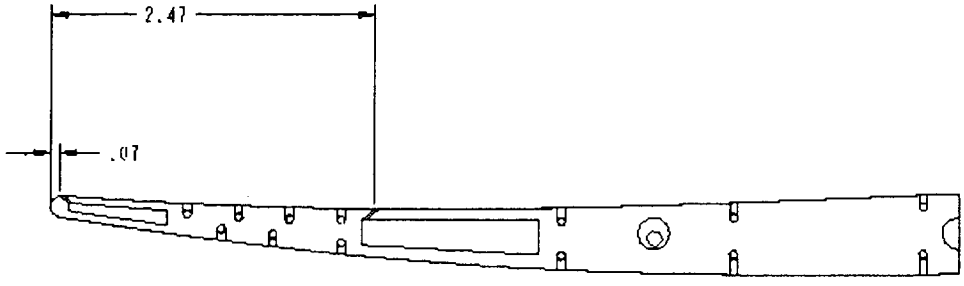

Figure 3.5: Boundary layer control cavity con□guration 2.

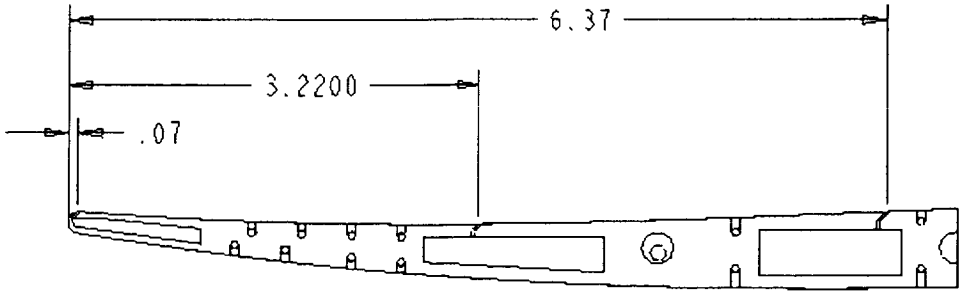

Figure 3.6: Boundary layer control cavity con□guration 3.

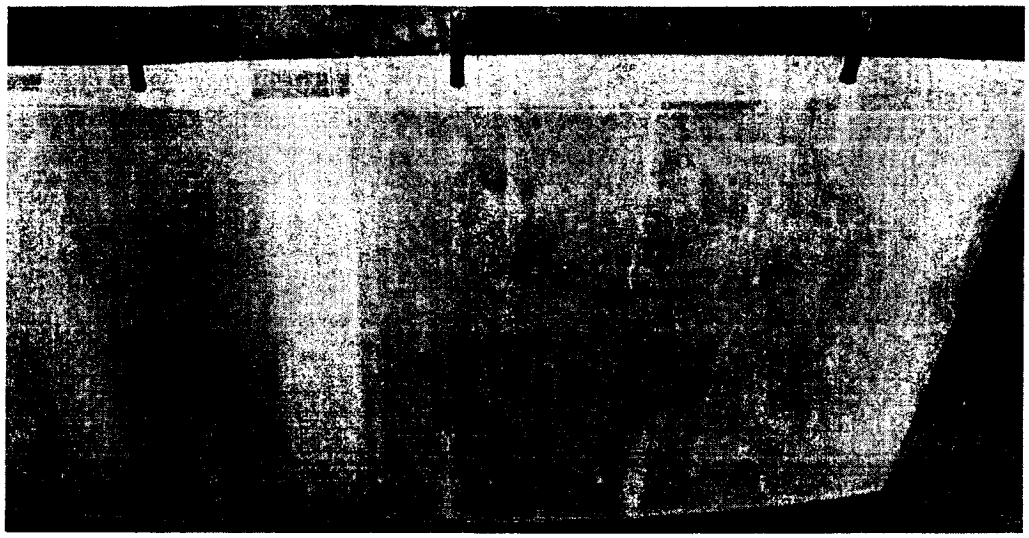

Figure 3.7: Photograph of airfoil section with cavity con□guration 1.

the cascade. Figure 3.9 compares the steady surface pressure coefficient for the no □ow control condition to the case where suction was applied to the middle and aft cavities for slot design 1. As illustrated in Figure 3.9, suction applied to the two cavities downstream of the leading edge did not provide much improvement from the baseline no □ow control data. However, moving the suction to the leading edge was found to have a dramatic in□uence on the steady surface pressure coefficient as illustrated in Figure 3.10.

Figure 3.10 shows the pressure coefficient at 5% chord has increased substantially over the baseline no □ow control data. This indicates an increased suction peak and a decrease in □ow separation. The pressure coefficient continues to decrease downstream of the 5% chord location to the values found for the no □ow control case in the 50% chord region.

3.4. Summary and Conclusions

A nine airfoil cascade test section was fabricated and installed in the University of Kentucky, Paducah wind tunnel. Three suction slot con□gurations were designed for □ow control. The University of Kentucky Stereo Lithography (SLA) machine, which is capable of making intricate three-dimensional parts was utilized

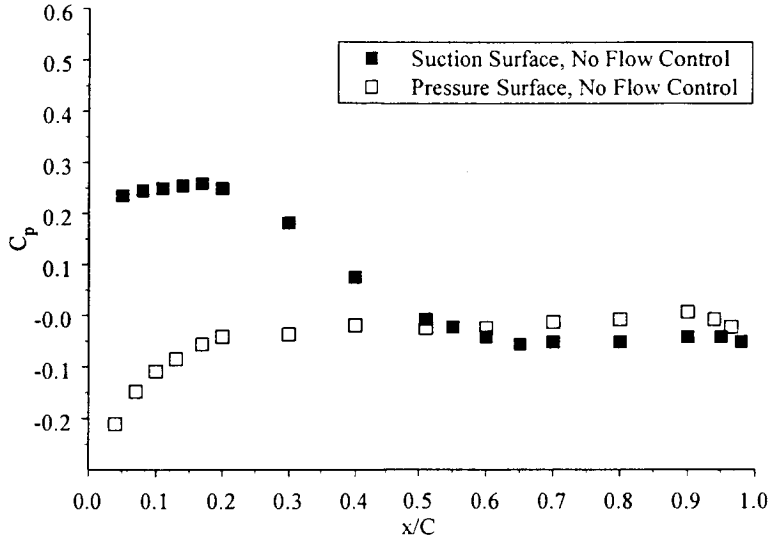

Figure 3.8: Airfoil midspan steady surface static pressure coefficient distribution without any □ow control.

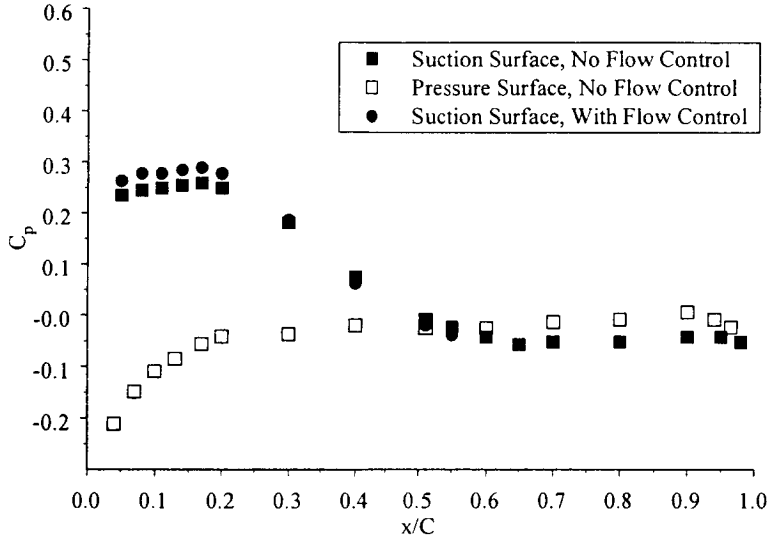

Figure 3.9: Airfoil midspan steady surface pressure coefficient distribution for suction applied at middle and last slots for cavity con□guration 1.

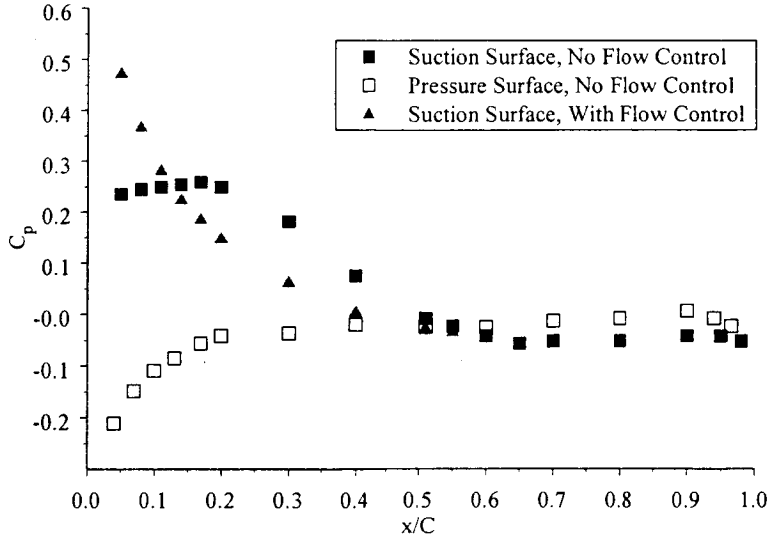

Figure 3.10: Airfoil midspan steady surface pressure coefficient distribution for suction applied to leading edge cavity for cavity con□guration 1.

to manufacture the cascade airfoils with the hollow cavities and slots at the desired locations. The cavities and slots were designed using three-dimensional solid modeling. The SLA machine used the output from the solid modeling software to manufacture the desired airfoil geometry. The three different cavity con□gurations were designed to quantify the in□uence of cavity entrance orientation and cavity location. These designs could be use for boundary layer suction or blowing. This could include the use of time dependent schemes for suction or blowing for □ow control.

Boundary layer suction was used on the suction surface of an advanced fan or compressor blade contour to control the separated □ow region in the leading edge region. This was accomplished through slots in the suction surface that were connected to hollow cavities within the airfoil cross-section. The air was suctioned from these cavities using vacuum type pumps.

Suction applied to the cavity with the entrance in the vicinity of the separation point was found to have the greatest impact on the steady surface pressure distribution. This is consistent with results found by previous investigators.

4. COMPUTATIONAL INVESTIGATION

With the advent of smart materials it is becoming possible to alter the structural characteristics of turbomachine airfoils. This change in structural characteristics can include, but is not limited to changes in the shape (morphing) of the airfoil. Through changes in the airfoil shape aerodynamic performance can be improved. Moreover, this technique has the potential to act as a flutter suppressant.

To assess the influence of the change in airfoil shape on stability the work-per-cycle will be evaluated for torsion mode oscillations. This will be accomplished as follows. From the simulations of the airfoil oscillating in a pitching motion around the mid-chord the first harmonic pressure coefficient can be quantified.

$$C_p = \frac{P_1(x)}{\rho V^2 \alpha_1} \tag{4.1}$$

The difference in pressure between the lower and upper surfaces yields the force exerted on the airfoil.

$$\Delta C_p(x) = C_{p_{lower}}(x) - C_{p_{upper}}(x) \tag{4.2}$$

The unsteady aerodynamic moment coefficient for thin airfoils is defined as

$$C_M = \int_0^1 \left(\frac{x_{pitch}}{C} - \frac{x}{C}\right) \Delta C_p \left(\frac{x}{C}\right) d\frac{x}{C} \tag{4.3}$$

where C is the airfoil chord and $x_{pitch}/C = 0.5$ for the NASA/P&W airfoil. The work done on the airfoil by the fluid per cycle of oscillation when the airfoil is oscillating in a pitching (torsion) motion is represented by cyclic integral of the real part of moment times the real part of the differential pitching angle as given below (Carta [23]). For sinusoidal motion

$$\widetilde{W} = \oint \mathrm{Re}\left[\widetilde{M}\right] d\,\mathrm{Re}\left[\widetilde{\alpha}\right] \tag{4.4}$$

and

$$\widetilde{\alpha} = \alpha_1 e^{i\omega t} \tag{4.5}$$

$$\widetilde{M} = \left(\widetilde{M}^R + i\widetilde{M}^I\right) e^{i\omega t} \tag{4.6}$$

where

i is the $\sqrt{-1}$

$\widetilde{M}^R$ is the real part of the complex valued unsteady aerodynamic moment

$\widetilde{M}^I$ is the imaginary part of the complex valued unsteady aerodynamic moment.

Substitution into the cyclic integral for the work per cycle and carrying out the integration yields

$$\widetilde{W} = \pi\alpha_1 \widetilde{M}^I. \tag{4.7}$$

This is the aerodynamic work being done on the airfoil. A positive value indicates unstable motion. Note that the aerodynamic work-per-cycle is proportional to the imaginary part of the unsteady aerodynamic moment coefficient, $\mathrm{Im}\left[C_M\right]$, with $\mathrm{Im}\left[C_M\right] > 0$ indicating instability. Hence, through examination of the integrand of the unsteady aerodynamic moment coefficient localized areas of the airfoil can be identified that contribute to airfoil instability. This type of information can be used to identify local flow physics with airfoil instability and will be used to direct the changes made in the shape of the airfoil.

In this work the integrand of the complex valued unsteady aerodynamic moment coefficient will be referred to as the Work Impulse and will be represented as C'_w

$$C'_w = \left(\frac{x_{pitch}}{C} - \frac{x}{C}\right) \Delta C_p \left(\frac{x}{C}\right)$$

4.0.1. Airfoil Geometry Modifications

For the baseline airfoil given in Table 2.1 and Figure 2.1, the camberline can be changed based on some preset constraints. There are two design variables used in this study to control airfoil shape, as illustrated in Figure 4.1. One is airfoil leading edge camberline angle (θ), and the other is airfoil leading edge camberline height from the reference point (δ). The Reference point is the lowest point along the airfoil camberline. For this study, the airfoil thickness distribution is held constant.

Figure 4.2 illustrates that there are three fundamental camberline shapes used in this investigation. These are:

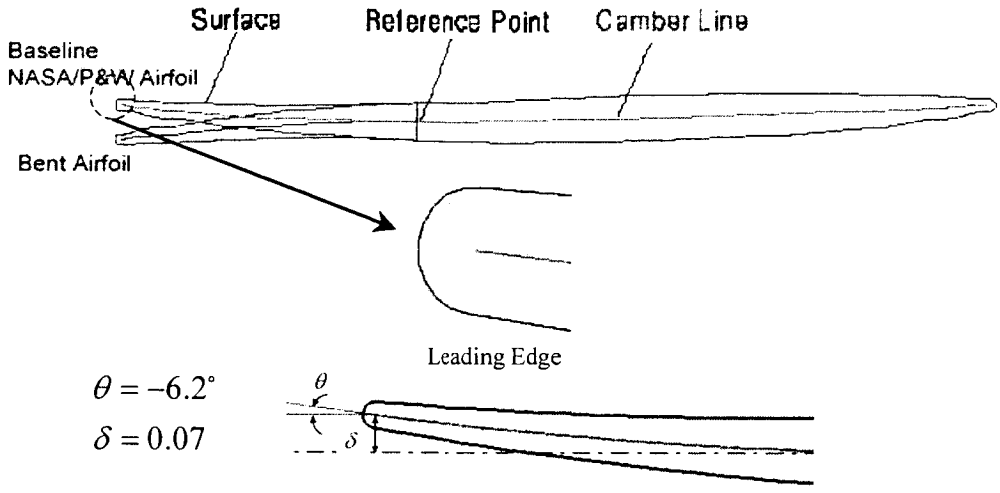

Figure 4.1: Baseline NASA/Pratt&Whitney airfoil shape.

1. The baseline camber case with $\theta = -6.2°$ and $\delta = 0.066$.
2. The zero leading edge camber case where $\theta = 0°$ and $\delta = 0$.
3. The mirror case where the camberline is a mirror image of the baseline camber case with $\theta = 6.2°$ and $\delta = -0.066$.

A polynomial, which is given below in Equation 4.8, is used to locate the leading edge for each of these airfoil cases. Additionally, given the desired δ and θ for a change in the airfoil front camber, Equation 4.8 also provided the initial guess for the location of the leading edge $(x_0,\ y_0)$ as will be discussed below.

$$y_{le}(x) = b_1 + b_2 x + b_3 x^2 \tag{4.8}$$

Now lets consider the front camberline of the airfoil. The front camberline of the airfoil is represented by the third order polynomial

$$y_{cl}(x) = a_1 + a_2 x + a_3 x^2 + a_4 x^3. \tag{4.9}$$

Four boundary conditions are used to find the coefficients a_1 through a_4. These boundary conditions are:

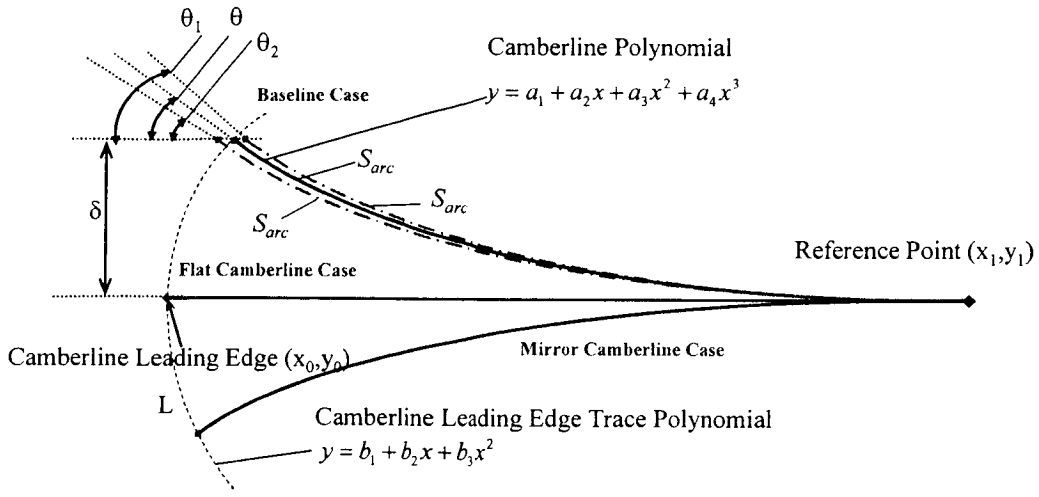

Figure 4.2: Schematic diagram illustrating method utilized to change the front camber of the NASA/P&W airfoil.

1. The camberline angle at the leading edge or nose point, θ
2. The leading edge offset or height from the Reference point, δ
3. The location of the Reference point, which is the lowest point on the baseline camberline
4. The camberline slope at the Reference point, which is zero.

These four boundary conditions will yield a camberline where the arc length, $S_{arc}|_{calculated}$, can be different than the original NASA/P&W (baseline) airfoil. In this investigation the camberline arc length, S_{arc}, was held constant at the baseline value. This was accomplished by using Equation 4.8 to define an initial value of the leading edge location ($x_{0_{initial}}$, $y_{0_{initial}}$) for the desired airfoil front camber shape, which is given by the design parameters δ and θ. The leading edge point is used with Equation 4.9

$$y_0 = a_1 + a_2x_0 + a_3x_0^2 + a_4x_0^3 = \delta + y|_{\delta=0} \tag{4.10}$$

along with the height of the reference point

$$y_1 = a_1 + a_2x_1 + a_3x_1^2 + a_4x_1^3, \tag{4.11}$$

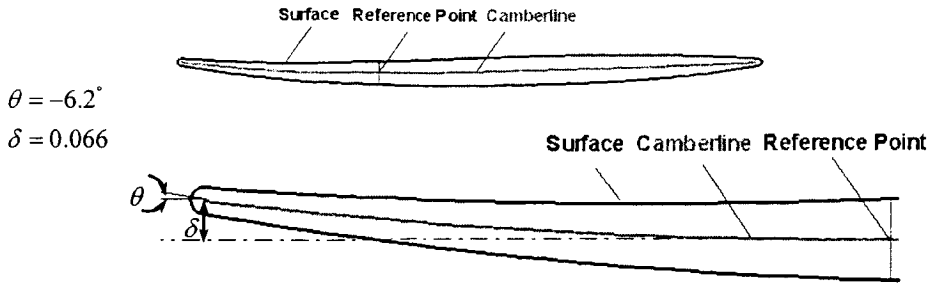

Figure 4.3: Baseline (NASA/P&W) airfoil shape with $\theta = -6.2°$ and $\delta = 0.66$.

the slope of the camberline at the leading edge

$$\tan(\theta) = a_2 + 2a_3 x_0 + 3a_4 x_0^2, \tag{4.12}$$

and the slope of the reference point

$$\tan(0°) = a_2 + 2a_3 x_1 + 3a_4 x_1^2 \tag{4.13}$$

to obtain the four coefficients a_1, a_2, a_3, and a_4.

This procedure may lead to the camberline arc length being larger than the baseline value. This results from the fact that x_0 is in□uence by the desired camberline offset, δ, and slope, θ. To determine the actual location of the leading edge, x_0, a search is conducted in the domain from $(x_{0_{initial}} - 0.1,\ x_{0_{initial}} + 0.5)$ to ensure that the camberline arclength matches the baseline airfoil value. This yields the □nal values of the coefficients a_1, a_2, a_3, and a_4.

Figures 4.3 through 4.5 illustrate variations in the airfoil leading edge shape for different values of the design variables of the camberline offset, δ, and slope, θ.

4.1. Grid Generation

TCGRID (Turbomachinery C-GRID) is a three-dimensional grid generator for turbomachinery developed at the NASA Glenn Research Center. It can generate both single-block grids and multi-block grids for a single periodic passage, which can be either C-grids or H-grids. An elliptic solver controls the grid spacing

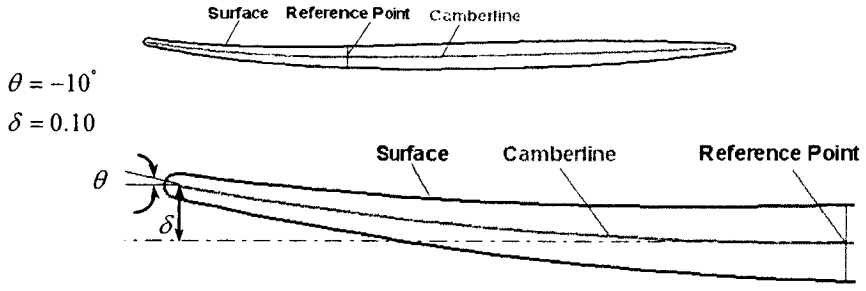

Figure 4.4: Airfoil shape for $\theta = -10°$ and $\delta = 0.10$.

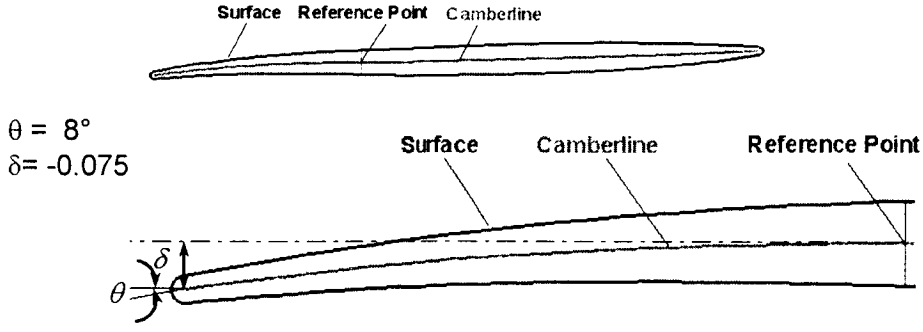

Figure 4.5: Airfoil shape for $\theta = 8°$ and $\delta = -0.075$.

Table 4.1: Turbulence model parameters.

Parameter	Baldwin-Lomax	Modified Baldwin-Lomax
κ	0.41	0.40
K	0.0168	0.0168
C_{cp}	1.6	1.216
C_{Kleb}	0.30	0.646
C_{wk}	0.25	1.00

and the angles at the blade surface and outer periodic boundary to generate blade-to-blade grids[24]. The linear cascade option was used to generate the two dimensional grids for an extruded section with the mid-span section grid being used.

A two-dimensional mid-span grid is shown in Figure 4.6. The grid size is $(i = 162) \times (j = 65)$. The first grid from the airfoil solid surface is 10^{-4} yielding an average $y^+ = 0.597$.

4.2. Computational Model

The computational model (**NPHASE**) analyzes two dimensional steady and unsteady flow. It is capable of analyzing both inviscid (Euler) and viscous (thin layer Navier-Stokes equations) flows. For unsteady flows a time marching method is used with a deforming computational mesh for oscillating airfoils. This fully nonlinear computational model uses multiple airfoil passages in order to satisfy the periodicity condition. A summary of the development efforts and current capabilities of this computational model is given by Swafford et al.[3] and Ayer and Verdon[22].

Turbulent flow is modeled using the Baldwin-Lomax[25] algebraic turbulence model. There is no transition model and the flow is considered fully turbulent starting at the airfoil leading edge. The modeling parameters in the Baldwin-Lomax model have been modified by previous investigators to achieve better agreement with the Cebeci and Smith model[26]. **NPHASE** was originally developed using the parameters published by Baldwin-Lomax[25] (except κ). For this work the model parameters were updated based on the work of Chima, Giel, and Boyle[27]. Table 4.1 presents the original parameters used in **NPHASE** and the modeling constants used in this investigation.

NPHASE is executed in a two-step process. First, the steady flow field is

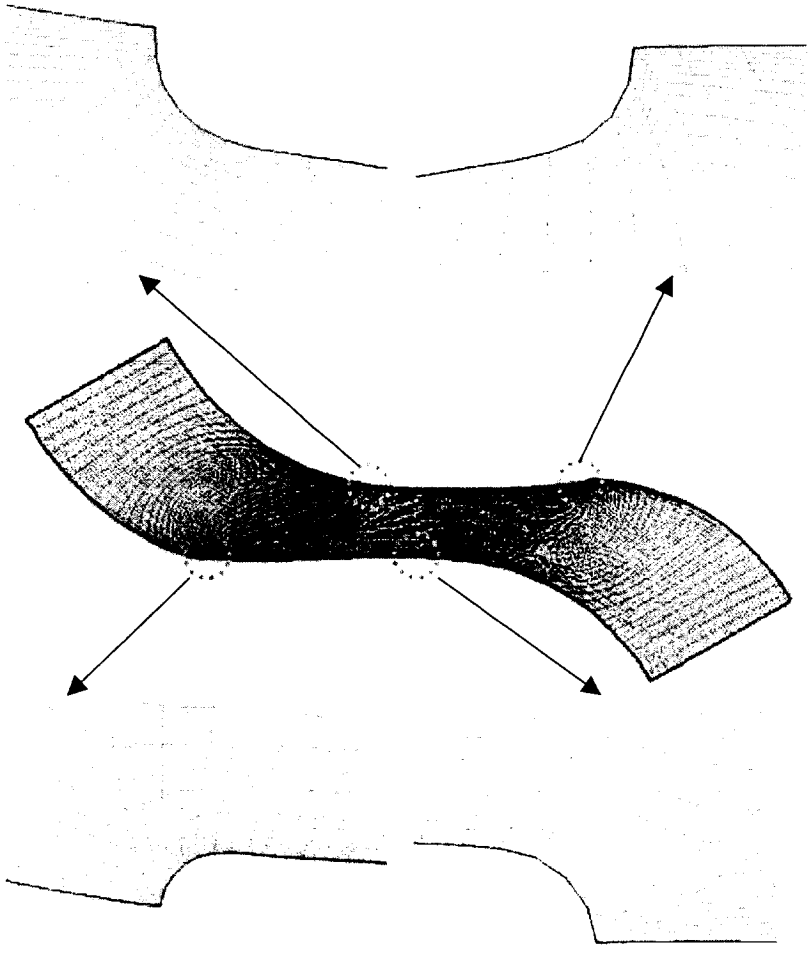

Figure 4.6: Two-dimensional baseline 165x65 grid.

determined. Once the steady □ow □eld is determined, the unsteady calculations can be initiated. For this research the unsteady calculations were for an airfoil oscillating in a pitching motion around the mid-chord of the airfoil.

4.3. Results

4.3.1. Flow Conditions

Results will be presented for the chordal incidence angles ($\overline{\alpha}$) of 0° and 10° at an inlet Mach number (M) of 0.5. Each chordal incidence angle was based on the cascade inlet angle relative to the airfoil chord-line (see Figure 2.1); upstream □ow angle measurements were not made during the experiments[10]. Unsteady data will be presented for a 180° interblade phase angle (σ) and a reduced frequency ($k = \frac{\omega C}{2V_{in}}$) of 0.4. For all cases the airfoils are oscillated in a pitching (torsional) motion about the mid-chord at an oscillation amplitude of 1.2°. All data-computation correlations are referenced by the experimental value of the chordal incidence angle and inlet Mach number. The Reynolds number was 0.9 *Million*.

The results will be presented in two parts. In the □rst part the low chordal incidence angle ($\overline{\alpha} = 0°$) will be considered with individual cases computed as listed below.

1. Steady and oscillating airfoil simulations are made using the original coordinates for the NASA/P&W airfoil, i.e. the baseline airfoil. This is referred to as the baseline case. Predictions are correlated with the experimental data.

2. Steady and oscillating airfoil simulations are made of an airfoil generated with the airfoil modi□cation routines for the leading edge camber angle ($\theta = -6.2°$) and leading edge camber height ($\delta = 0.066$) for the NASA/P&W airfoil. This airfoil is referred to as the simulated baseline airfoil. These results are correlated with the baseline case to validate the airfoil modi□cation methodology. This case is called the simulated baseline case.

3. To study the in□uence of the design parameters θ and δ on stability, the leading edge camber angle is set to 0° and the leading edge camber height is set to 0 and an airfoil is generated without any camber in the leading edge region. Steady and oscillating airfoil simulations of this airfoil are

compared with the baseline case. The work impulse function is used to show an improvement in the predicted stability in the airfoil leading edge region compared to the baseline airfoil. The leading edge region is the region between the leading edge (nose point) and mid-chord.

The second part considers the high chordal incidence angle ($\overline{\alpha} = 10°$). The individual cases considered are listed below.

1. As for the small mean incidence operating condition, steady and oscillating airfoil simulations are made using the original coordinates for the NASA/P&W airfoil, i.e. the baseline airfoil. Predictions are correlated with the experimental data.

2. A search was conducted for minimum changes in the leading edge camber height (δ) that yielded predicted flutter stability in the leading edge region holding the leading edge camber angle constant at $-6.2°$. The minimum change in δ was taken to be the value that yielded a maximum work impulse in the leading edge region of zero. Steady and oscillating airfoil simulations for the final airfoil shape are correlated with the baseline airfoil. The improvement in the predicted airfoil stability is illustrated through a comparison with the baseline airfoil using the work impulse function.

3. As for the small mean incidence condition, steady and oscillating airfoil solutions were generated for airfoil resulting from a leading edge camber angle of 0° and a leading edge camber height of 0. The work impulse function is used to show an improvement in the predicted stability in the airfoil leading edge region compared to the baseline airfoil.

Two-dimensional grids from TCGRID are used with 162 grids in the axial direction and 65 grids in the circumferential direction (162×65). To establish grid independence results from the 162×65 grid are compared with results from a 181×81 grid and a 301×121 grid for most cases.

4.3.2. Baseline Case: Steady Flow for $\overline{\alpha} = 0°$

The baseline case uses the original surface coordinates from the NASA/P&W airfoil. The airfoil shape is illustrated in Figure 4.3.

The cascade inlet flow angle was varied until the best match was found between the steady chordwise pressure coefficient data $\left(\overline{C}_p = \frac{P_{in} - P}{\rho_{in} V_{in}^2}\right)$ and the predictions.

Table 4.2: In□uence of grid resolution on reattachment point for the low incidence angle case.

Airfoil Case	Grid Size	Separation Point	Reattachment Point
NASA/P&W	181×81	$0.005C$	$0.067C$
NASA/P&W	301×121	$0.005C$	$0.051C$
NASA/P&W	162×65	$0.005C$	$0.105C$

This resulted in a 1° chordal incidence angle being used in all the presented □ow solutions. Computations were conducted on three grids. The grid sizes are 181×81, 301×121, and 162×65. The convergence history for the lift coefficient and the absolute value of the average density residual are presented in Figures 4.7 and 4.8, respectively.

For each grid it is seen that the average density residual is less than 10^{-8} and the lift coefficient has stabilized. These are indications of a converged solution. Future results will present the convergence history of the lift coefficient for steady □ow computations with the convergence history of the average density residual being typical of what is seen in this case.

Figure 4.9 presents the correlation of the predicted steady surface pressure coefficient with the experimental data. The correlation of the predictions with the experimental data shows there is a deviation with the experimental data along the upper (suction) surface in the leading edge region where the □ow is separated. The larger grid gives a slightly higher pressure coefficient in the separation region, but yields the same separation point as the 181×81 grid.

The predicted reattachment point for the three grids is given in Table 4.2. The extent of the computed separation zone is shown in Figure 4.10, which presents contours of ρu.

For the 181×81 and 301×121 grids, the reattachment point is at 6.7% and 5.1% of chord respectively, which are only slightly different, whereas the separation point is at 10.5% of chord for the relatively small size grid. For computational accuracy, a large size grid is preferred. However, for computational efficiency, a small size of grid is preferred. To guarantee computational accuracy and efficiency, a grid size of 162×65 is judged sufficient for the computations presented below.

4.3.3. Baseline Case: Unsteady Flow for $\overline{\alpha} = 0°$

The effect of time step was investigated for this case. The grid size of 181×81 was used for this study. Figure 4.11 presents the predicted work-per-cycle for 512

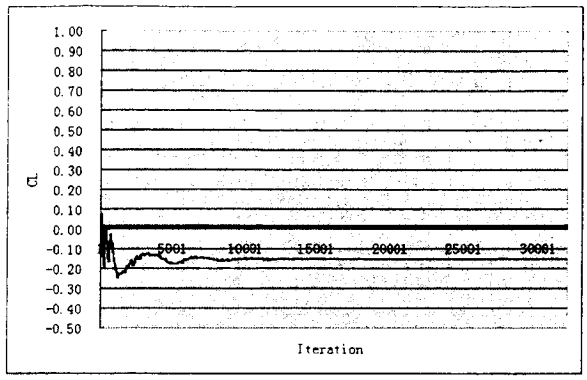

(a) Grid size 301x121

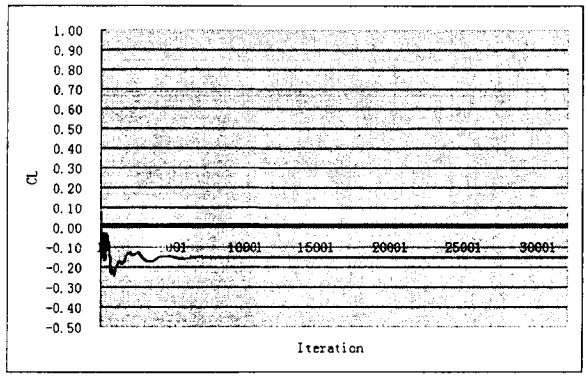

(b) Grid size 181x81

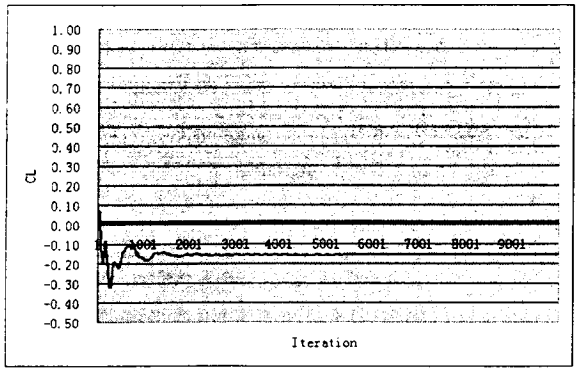

(c) Grid size: 162x65

Figure 4.7: Lift coefficient convergence history for the low incidence baseline case.

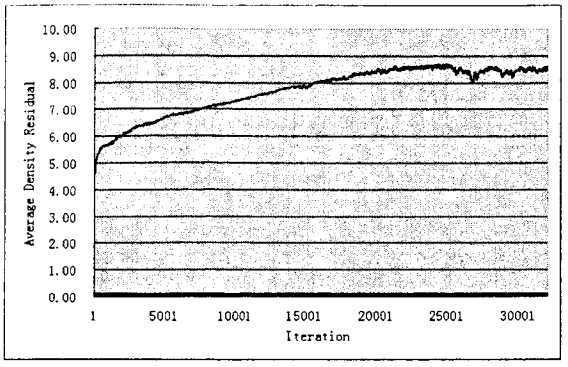

(a) Grid size: 301x121

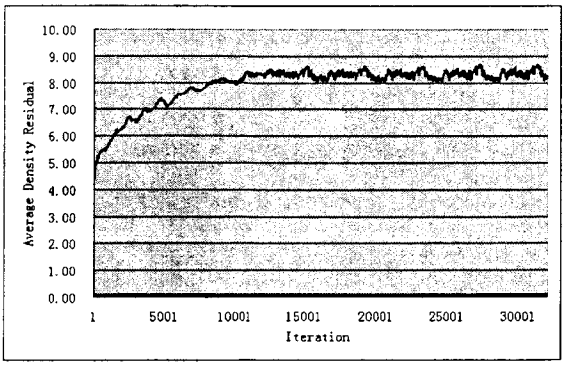

(b) Grid size: 181x81

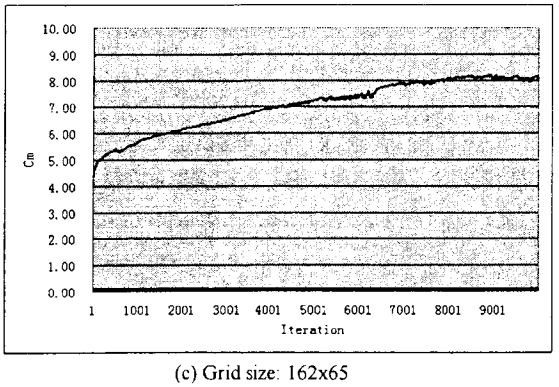

(c) Grid size: 162x65

Figure 4.8: Absolute value of the average density residual convergence history for the low incidence baseline case.

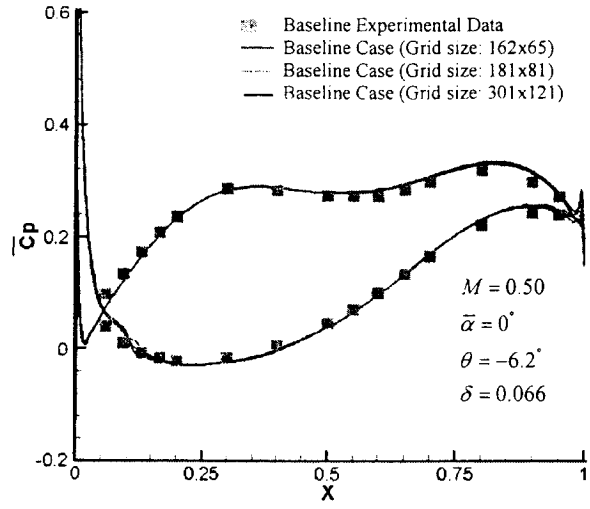

Figure 4.9: Low incidence baseline case steady surface pressure coefficient distribution

points per cycle, 1024 points per cycle, and 2048 points per cycle. The presented results indicate that the work-per-cycle is constant after the second cycle. This is further illustrated in Figure 4.12, which presents the unsteady moment coefficient.

Figure 4.13 presents the predicted work-per-cycle for 162 × 65 grid size, 181 × 81 grid size, and 301 ×121 grid size. As shown above, these results indicate that the work-per-cycle is constant after the second oscillation cycle and there are only slight differences in the work-per-cycle with grid size. In addition, for this □ow condition 1024 points per cycle is sufficient for the unsteady simulations.

The □rst harmonic pressure coefficients are shown in Figure 4.14. The lower surface response is dominated by $Re(Cp)$ forward of mid-chord. The imaginary part of the lower surface is underpredicted. There is good agreement between the experimental data and the predictions for the upper surface. All three grid sizes show good agreement with each other. Also, the predictions show trendwise agreement with the experimental data.

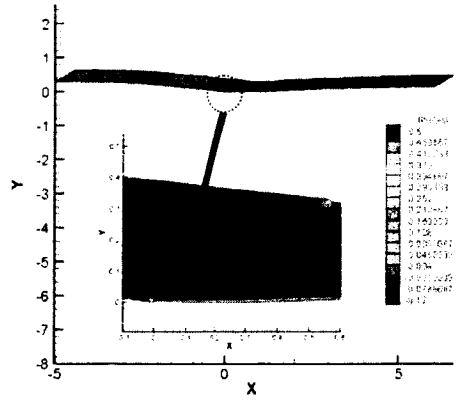

(a) Grid size: 181x81

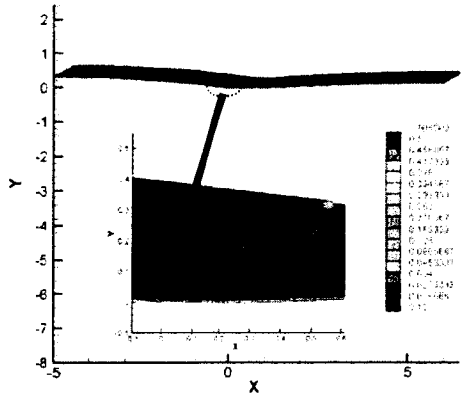

(b) Grid size: 301x121

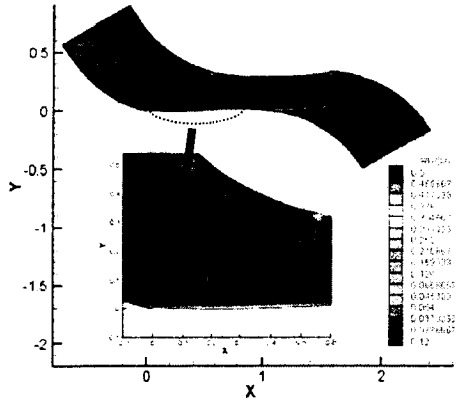

(c) Grid size: 162x65

Figure 4.10: Low incidence baseline case ρu contours.

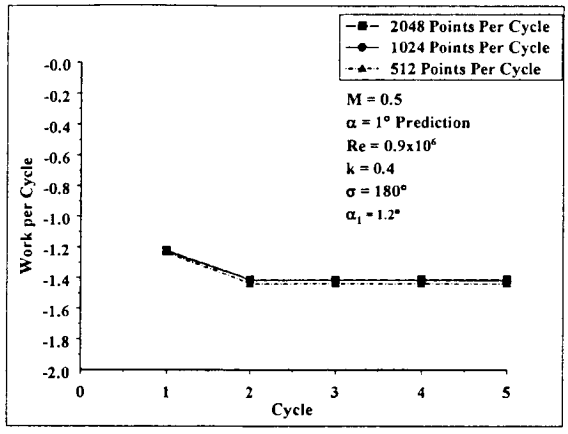

Figure 4.11: In□uence of time step on work-per-cycle for the low incidence baseline case.

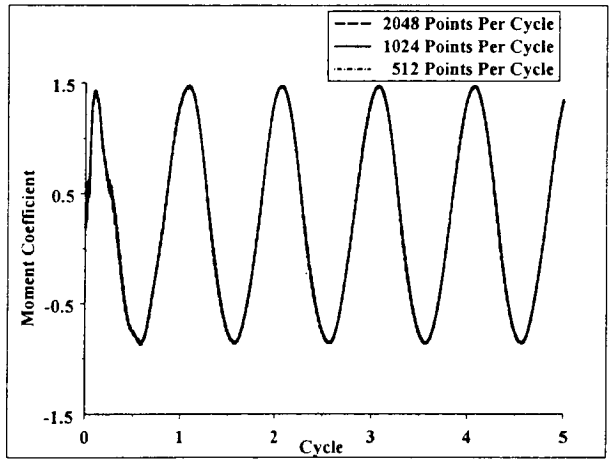

Figure 4.12: In□uence of time step on unsteady aerodynamic moment coefficient for the low incidence baseline case.

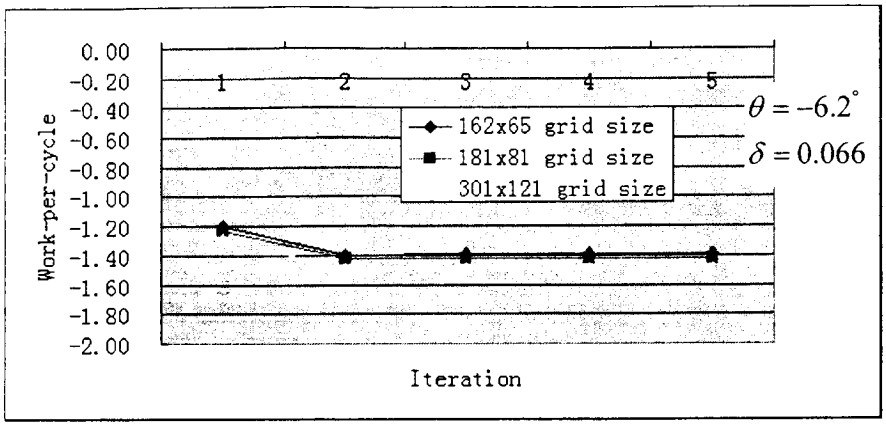

Figure 4.13: Low incidence angle case work-per-cycle

4.3.4. Baseline Case and Simulated Baseline Case: Steady Flow for $\overline{\alpha} = 0°$

The baseline case uses the original airfoil surface coordinates, see Figure 4.3. The simulated baseline case uses airfoil surface coordinates generated by the airfoil surface generation code as illustrated in Figure 4.15.

The simulated baseline case had a leading edge camber angle of $-6.2°$ and $\delta = 0.066$. Once the simulated baseline case is veri□ed, airfoils can be modi□ed to get pro□les where the unstable work impulse is stabilized in the leading edge region.

The 1° chordal incidence angle, which was established in the previous section as giving the best correlation with the experimental results, was used for these solutions. The convergence history for the lift coefficient is presented in Figure 4.16. Figure 4.16 shows that after the initial transients from the assumed uniform □ow used for the initial condition, the lift coefficient reaches a steady value after approximately 6000 iterations.

Figure 4.17 presents the correlation of the predicted steady surface pressure coefficient with the experimental data. For the simulated baseline case, the reattachment point was predicted to be at approximately 8.19% chord, which is slightly lower than the baseline case (see Table 4.2). As illustrated below, there is much better correlation between the two grid sizes for the unsteady □ow computations.

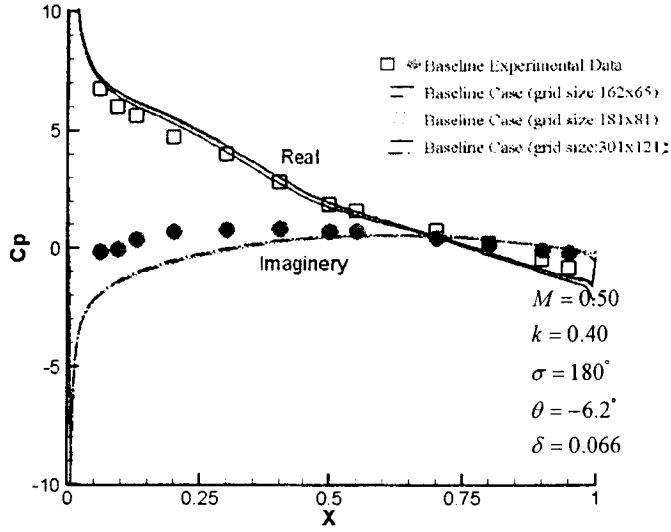

(a) Lower surface

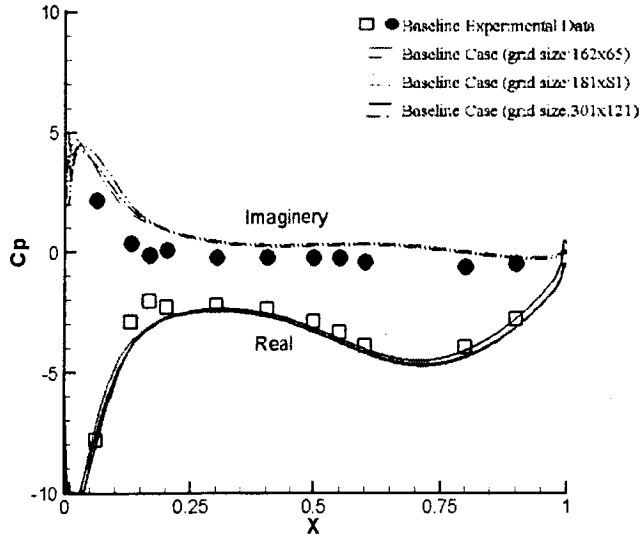

(b) Upper surface

Figure 4.14: Low incidence baseline case □rst harmonic unsteady surface pressure coefficient distribution.

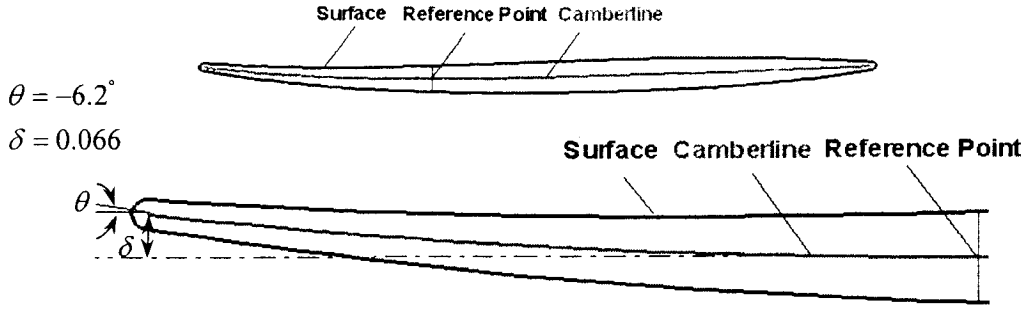

Figure 4.15: Simulated baseline (NASA/P&W) airfoil shape.

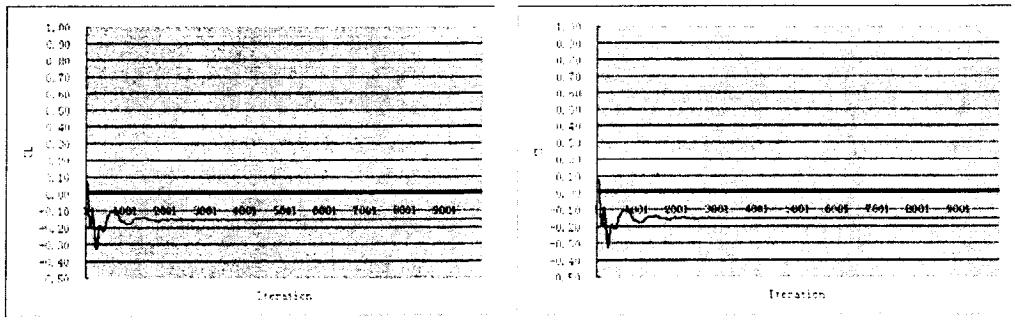

(a) Baseline Case

(b) Simulated Baseline Case

Figure 4.16: Lift coefficient convergence history for baseline and simulated baseline cases for the low incidence angle operating condition.

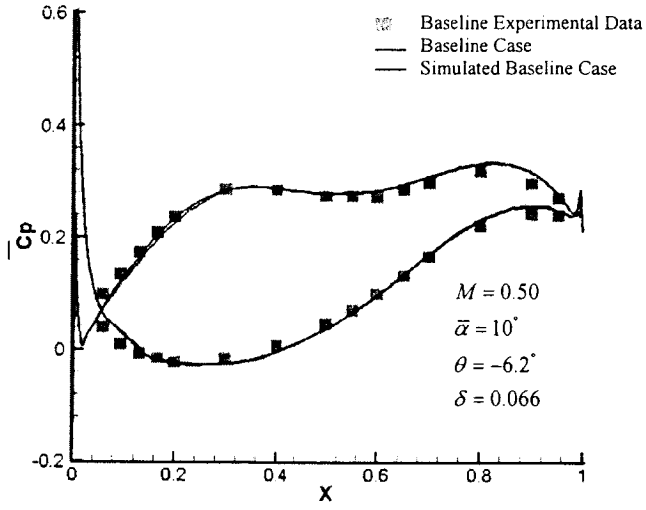

Figure 4.17: Baseline and simulated baseline case steady surface pressure coefficient distribution for the low incidence angle case

4.3.5. Baseline Case and Simulated Baseline Case: Unsteady Flow for $\overline{\alpha} = 0°$

For the unsteady flow computation, the unsteady moment coefficient (C_M) converges to a sinusoidal type wave shape for both the baseline case and the simulated baseline case, as shown in Figure 4.18. The work-per-cycle converged after two cycles with the simulated baseline case having a slightly higher value, as illustrated in Figure 4.19.

The first harmonic unsteady surface pressure coefficient is presented in Figure 4.20. Both configurations have similar correlations with the experimental data as was found above. Also, note that the baseline case and the simulated baseline case have good correlation with each other.

For the work impulse, both computational predictions are slightly below the experimental data, but exhibit good trendwise agreement as shown in Figure 4.21. The two computations exhibit excellent correlation with each other. From the work impulse for the experimental data, it can be clearly seen, the baseline case is unstable in leading edge region.

These results validate the airfoil geometry generation routines.

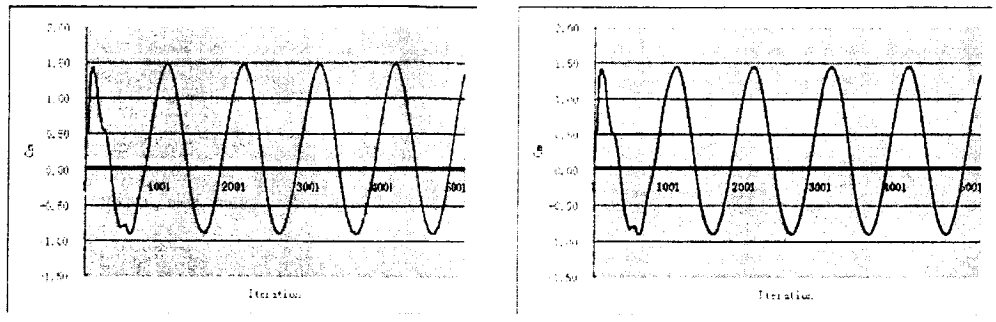

(a) (b)

Figure 4.18: Low incidence time dependent moment coefficient for the low incidence angle case: a) Baseline airfoil shape, and b) Simulated baseline airfoil shape.

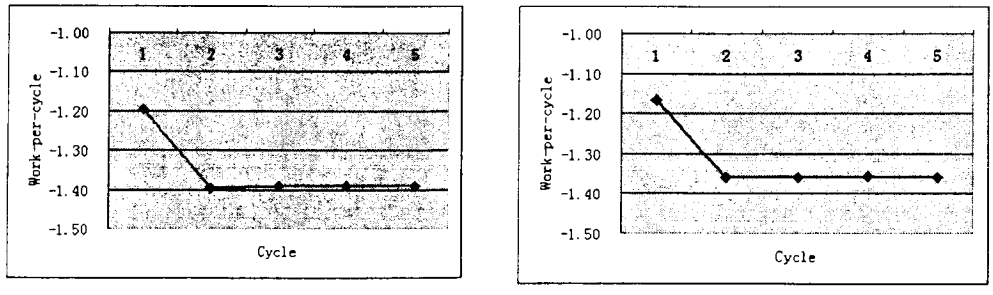

(a) (b)

Figure 4.19: Low incidence operating condition work-per-cycle: a) Baseline airfoil shape, and b) Simulated baseline airfoil shape.

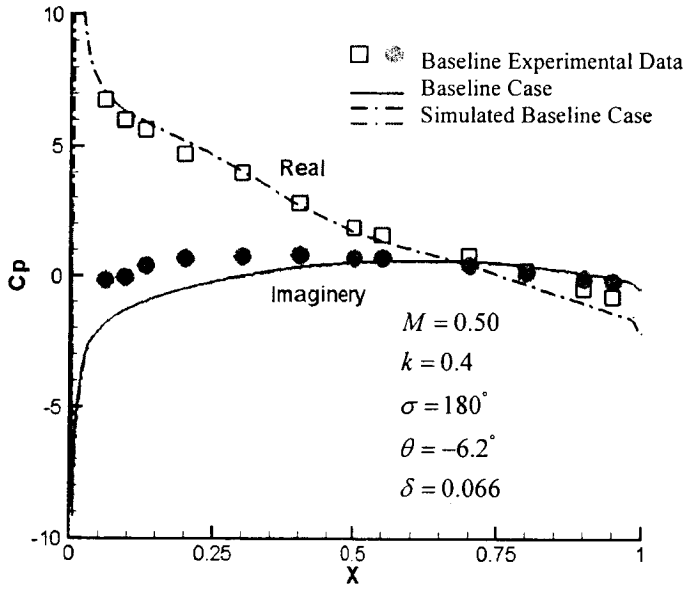

(a) Lower surface

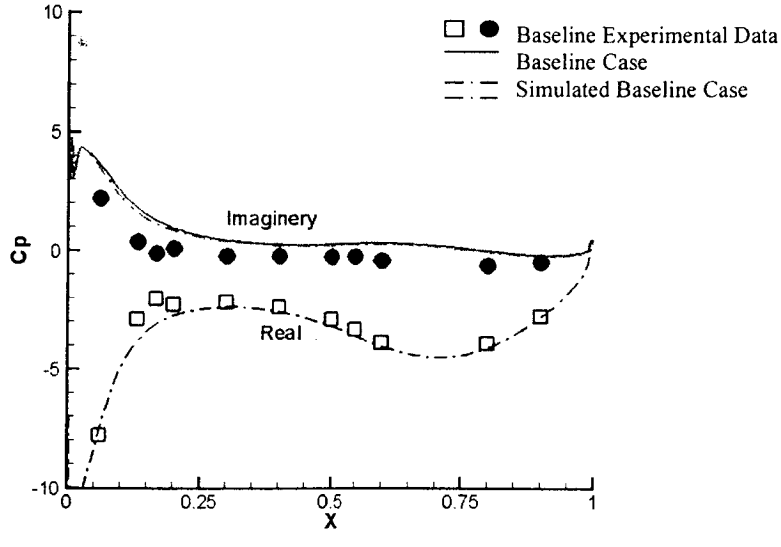

(b) Upper surface

Figure 4.20: Baseline and simulated baseline case first harmonic surface pressure coefficient distribution for the low incidence angle operating condition.

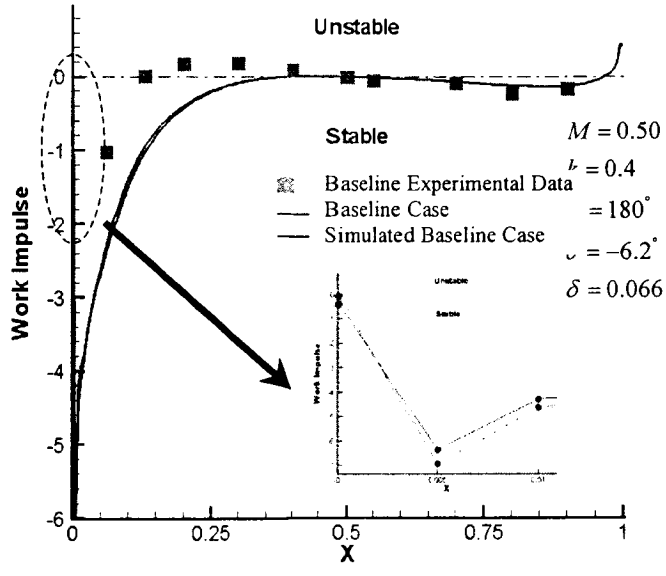

Figure 4.21: Baseline and simulated baseline case work-impulse for the low incidence angle operating condition.

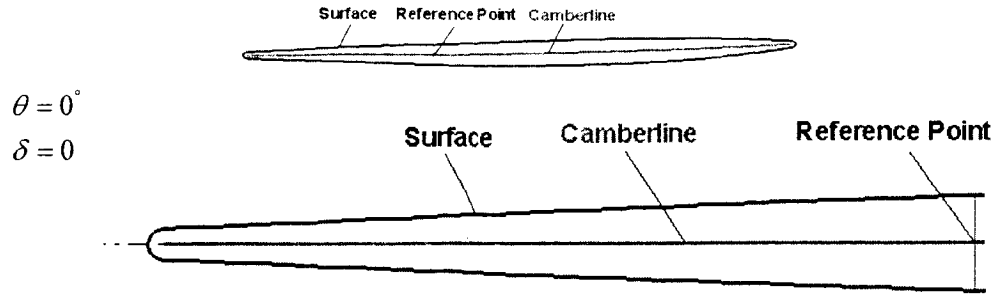

Figure 4.22: Airfoil shape for the $\theta = 0°$ and $\delta = 0$ case.

4.3.6. $\theta = 0°$ and $\delta = 0$ Case: Steady Flow for $\overline{\alpha} = 0°$

The case $\theta = 0°$ and $\delta = 0$ is the case that yields a stable work impulse function with both leading edge camber height changes and leading edge camber angle changes, see Figure 4.22. The lift coefficient convergence history is shown in Figure 4.23, which indicates the steady □ow solution has converged.

Figure 4.24 shows a dramatic change for the $\theta = 0°$ and $\delta = 0$ airfoil steady surface pressure coefficient $\overline{C}_p$ compared with experimental data and baseline case. The $\overline{C}_p$ increases in the leading edge region for both the pressure and suction surfaces and decreases along the chord for the suction surface compared with baseline case. Additionally, there is good agreement between the two different sized grids.

4.3.7. $\theta = 0°$ and $\delta = 0$ Case: Unsteady Flow for $\overline{\alpha} = 0°$

For airfoil oscillation, the unsteady moment coefficient converges to a sinusoidal wave type shape as shown in Figure 4.25, and the work-per-cycle converges to a cycle independent value after two oscillation cycles, see Figure 4.26. This indicates the simulation has converged to a steady oscillatory solution.

Figure 4.27 shows a distinct difference between the baseline case and the $\theta = 0°$ and $\delta = 0$ case for the unsteady surface pressure coefficient in the leading edge region. Furthermore, there is good agreement between the different size grids. The work impulse Figure 4.28, the $\theta = 0°$ and $\delta = 0$ case is stable in the leading edge region.

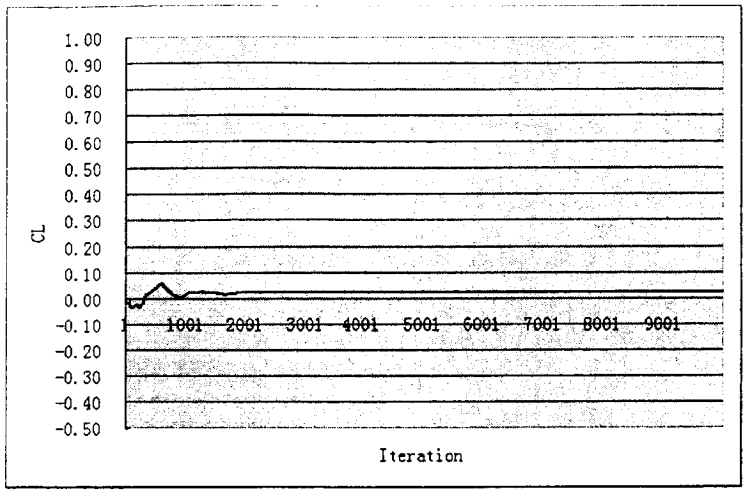

Figure 4.23: Lift coefficient convergence history for the low incidence operating condition for the $\theta = 0°$ and $\delta = 0$ airfoil.

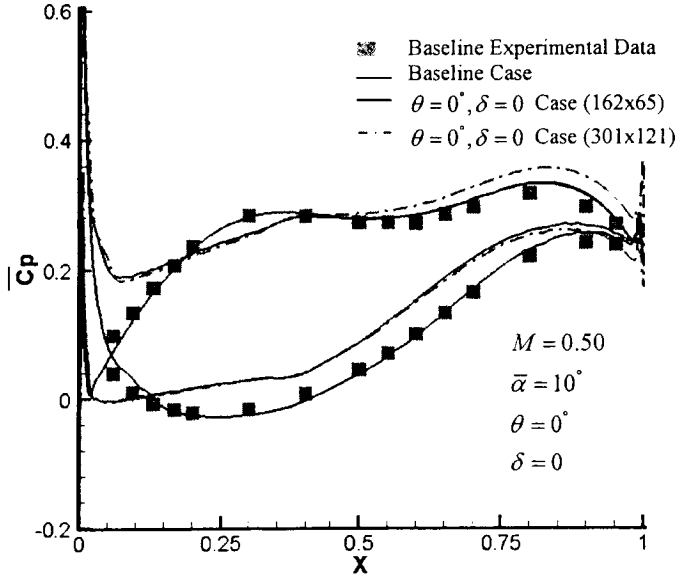

Figure 4.24: Low incidence $\theta = 0°$ and $\delta = 0$ case steady surface pressure coefficient distribution.

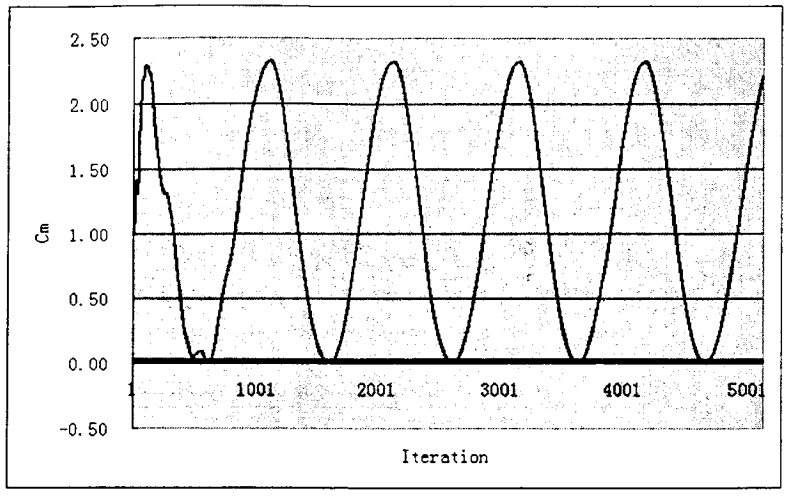

Figure 4.25: Time dependent moment coe□cient for the low incidence $\theta = 0°$ and $\delta = 0$ case.

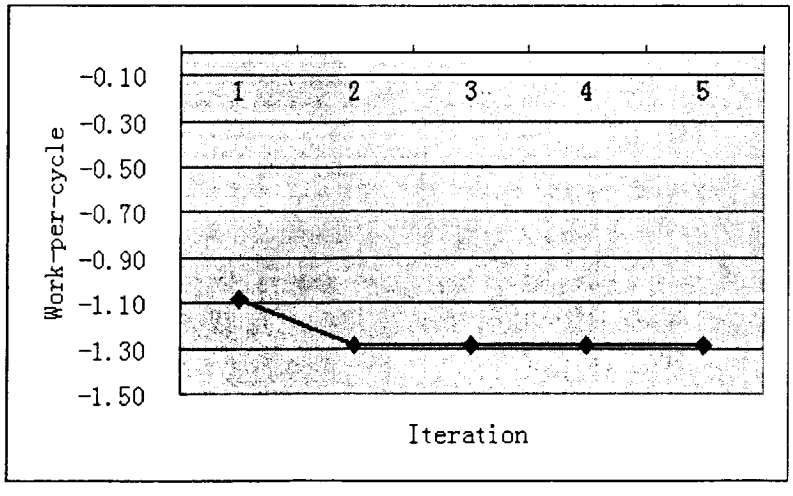

Figure 4.26: Work-per-cycle for the low incidence $\theta = 0°$ and $\delta = 0$ case.

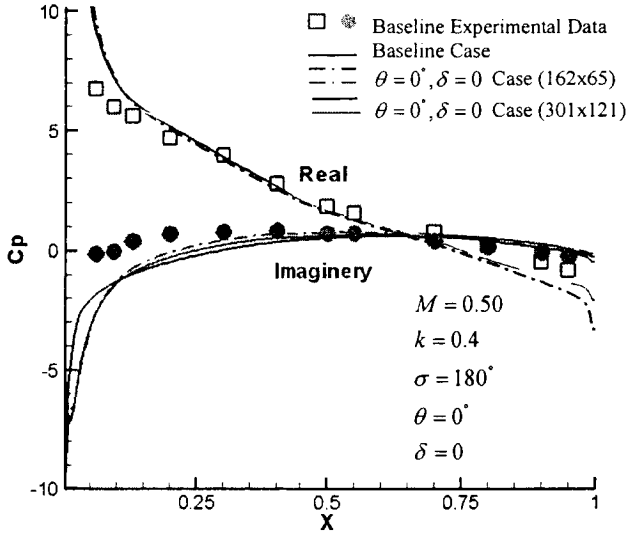

(a) Lower surface

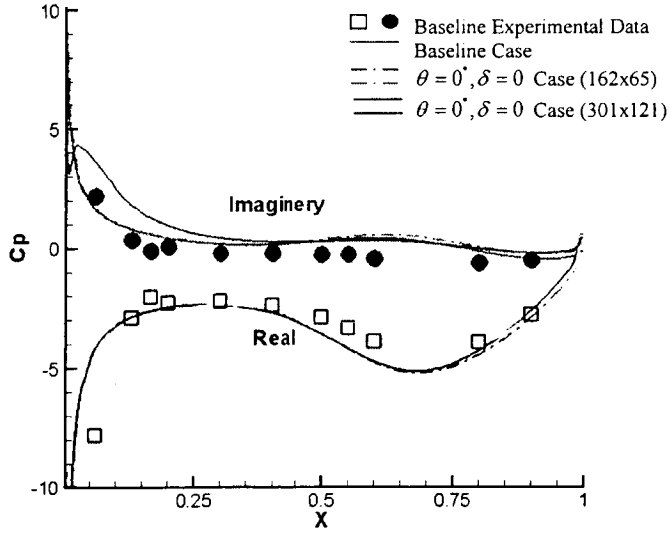

(b) Upper surface

Figure 4.27: First harmonic surface pressure coefficient distribution for the low incidence $\theta = 0°$ and $\delta = 0$ case.

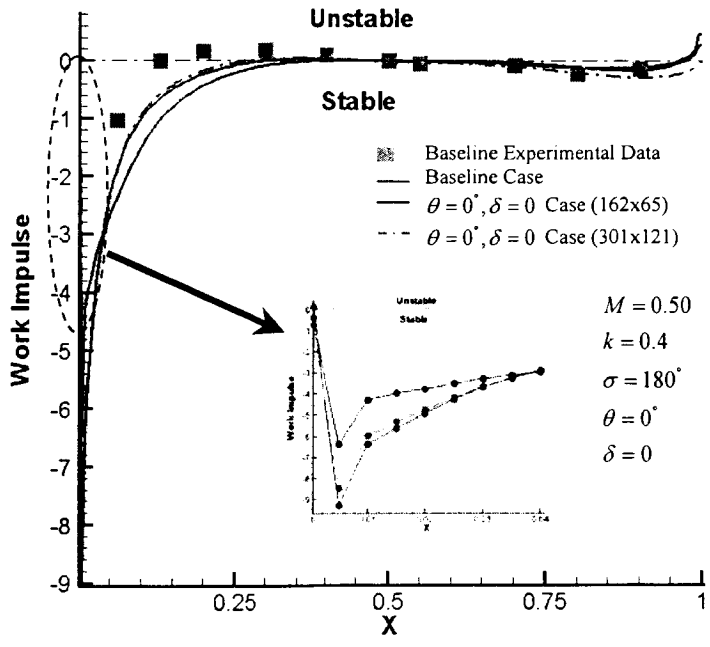

Figure 4.28: Work-impulse for the low incidence $\theta = 0°$ and $\delta = 0$ case.

As depicted in Figure 4.29, for the 162 × 65 grid the □ow separation point is at 0.9% chord and the □ow reattachment point is at 1.45% chord, and for the 301 × 121 grid the □ow separation point is at 0.9% chord and the □ow reattachment point is at 1.32% chord. This is compared with the baseline case for the 301 × 121 grid, which had a reattachment point is 5.1% chord. Hence, the □ow separation region is signi□cantly decreased.

This study at the lower incidence angle has shown that the □utter stability in the leading edge region can be improved through changes in the front camber of the airfoil. Therefore, the more challenging case for the large mean incidence angle condition will now be considered where the suction surface leading edge is highly loaded and a large separated □ow region is present.

4.3.8. Baseline Case: Steady Flow for $\overline{\alpha} = 10°$

The baseline case uses the original airfoil surface coordinates. The airfoil contour is illustrated in Figure 4.3.

The cascade inlet □ow angle was varied until the best match was found between the steady chordwise pressure coefficient data $(\overline{C_p})$ and the predictions. This resulted in a 7.5° chordal incidence angle being used in all the presented □ow solutions. Computations were conducted using the same three grid sizes as for the small mean incidence angle case. The lift coefficient convergence history for the grid sizes of 181 × 81, 301 ×121, and 162 × 65 is presented in Figure 4.30.

Figure 4.31 presents the correlation of the predicted steady surface pressure coefficient with the experimental data. The correlation of the predictions with the experimental data shows there is a deviation with the experimental data along the upper surface in the leading edge region where the □ow is separated. The larger grid gives a slightly higher pressure coefficient in the separation region, but yields the same reattachment point as the 181x81 grid.

Flow visualization at mid-span in the cascade indicated the □ow was separated from the leading edge to about 40% of chord. The predicted reattachment point for the three grids is given in Table 4.3. The deviation of the predicted reattachment point with the experimental data is attributed to the turbulence model and the lack of a transition model. The extent of the computed separation zone is shown in Figure 4.32, which presents contours of ρu.

For the 181 × 81 and 301 × 121 grids, the reattachment point is at 50% chord while the reattachment point is at 53.6% chord for the 162 × 65 grid. As found previously, for computational efficiency the grid size of 162 × 65 is sufficiently

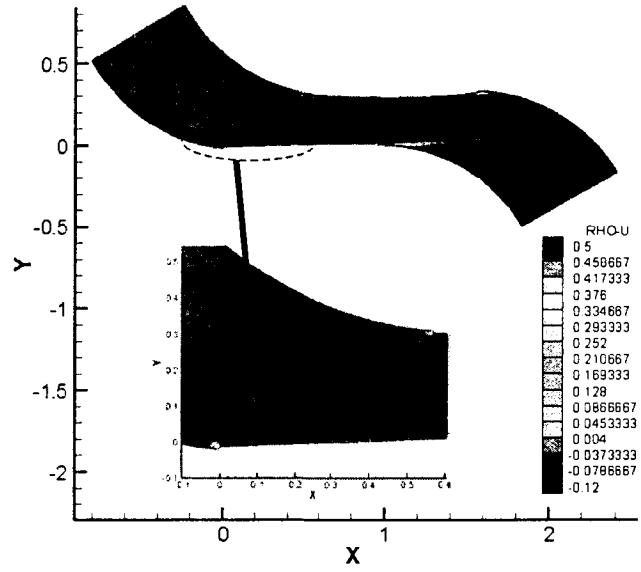

(a) Grid size: 301x121

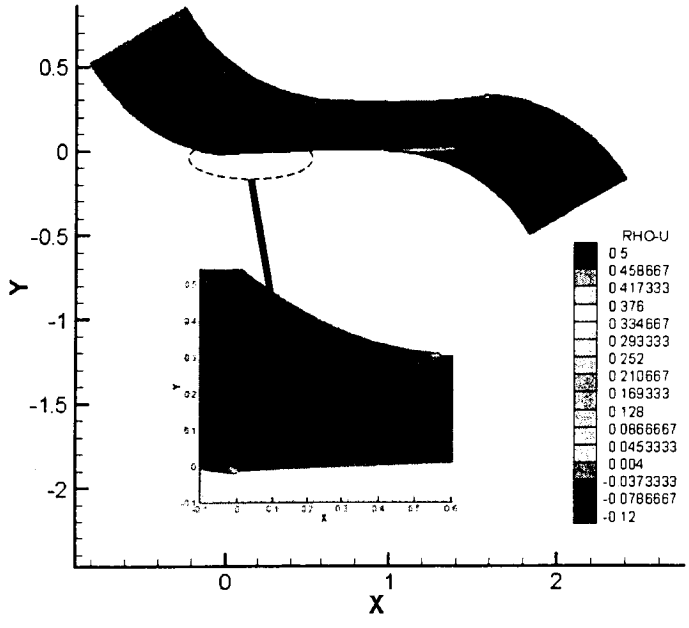

(b) Grid size:162x65

Figure 4.29: Low incidence $\theta = 0°$ and $\delta = 0$ airfoil case ρu contours.

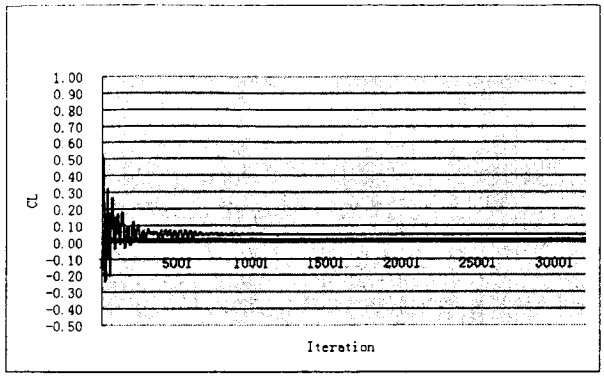

(a) Grid size: 301x121

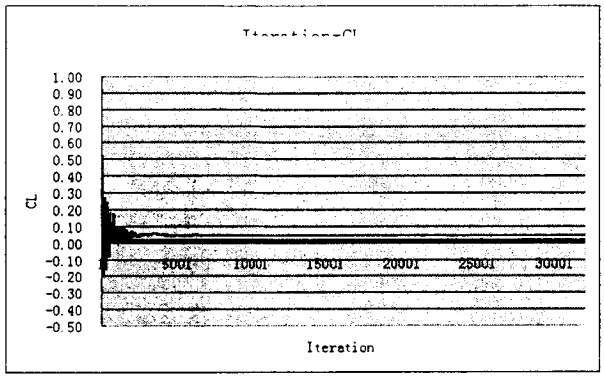

(b) Grid size: 181x81

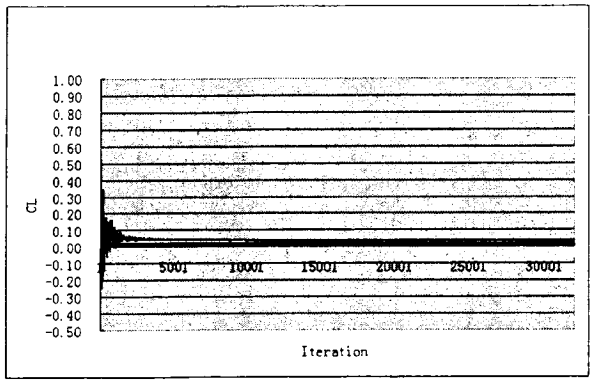

(c) Grid size: 162x65

Figure 4.30: Lift coefficient convergence history for the high incidence baseline case.

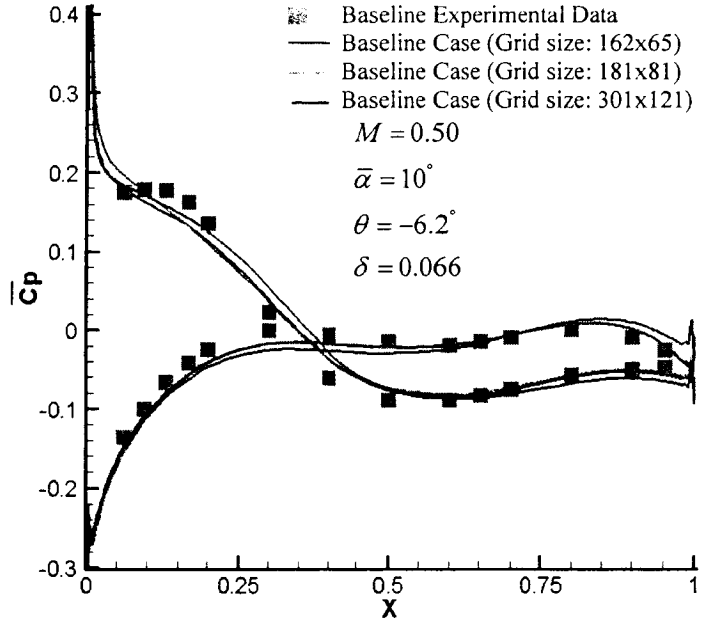

Figure 4.31: High incidence baseline case steady surface pressure coefficient distribution.

Table 4.3: Influence of grid resolution on reattachment point for the high incidence angle case.

Airfoil Case	**Grid Size**	**Separation Point**	**Reattachment Point**
NASA/P&W	181×81	$0.005C$	$0.500C$
NASA/P&W	301×121	$0.005C$	$0.500C$
NASA/P&W	162×65	$0.005C$	$0.536C$

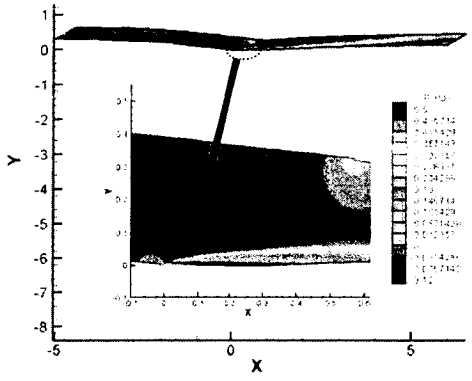

(a) Grid size: 181x81

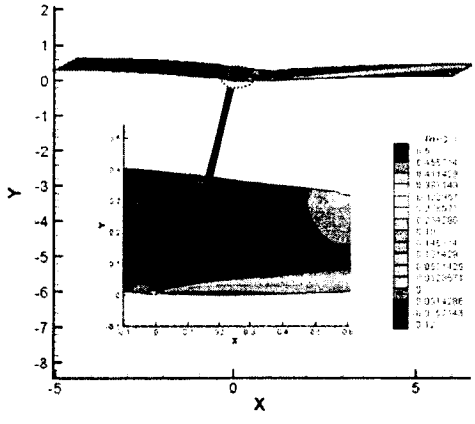

(b) Grid size: 301x121

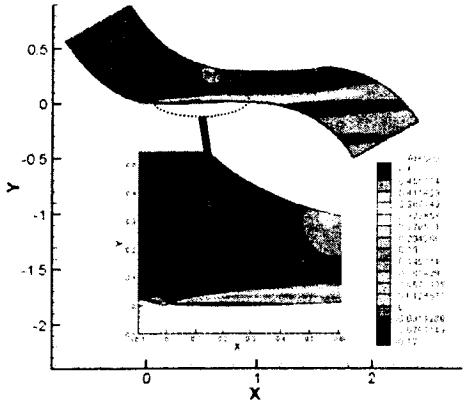

(c) Grid size: 162x65

Figure 4.32: High incidence baseline case ρu contours.

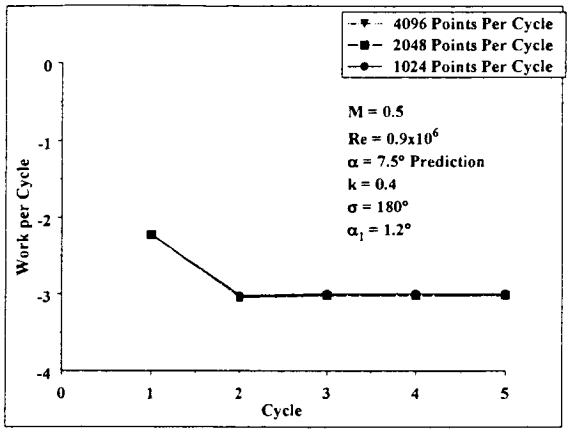

Figure 4.33: Work-per-cycle for high incidence baseline case.

accurate for the this study.

4.3.9. Baseline Case: Unsteady Flow for $\overline{\alpha} = 10°$

The influence of time step size on the unsteady simulations was also investigated for the large mean incidence angle case. The grid size of 181×81 was used for this study. Figure 4.33 presents the predicted work-per-cycle for 1024 points-per-cycle, 2048 points-per-cycle, and 4096 points-per-cycle. These results indicate that the work-per-cycle is constant after the second cycle and there are negligible differences in the work-per-cycle with time-step size for the values selected. Furthermore, for this flow condition 1024 points-per-cycle is sufficient for the unsteady simulations. Thus 1024 points-per-cycle was used for all subsequent unsteady simulations.

The first harmonic pressure coefficients are shown in Figure 4.34. The imaginary part of the lower surface is underpredicted. The upper surface pressure coefficients are influenced by the separation region with large pressure fluctuations over the first half of the airfoil. Similar results have been found by Sidén[5] when simulating subsonic unsteady separated flow generated from mid-chord pitching oscillations at large mean incidence angles for the Fifth Standard Configuration[28]. The reported results exhibited larger predicted pressure fluctuations in the separation

zone than the experimental data, as illustrated for the present case.

The predictions do show trendwise agreement with the experimental data. While the magnitudes are overpredicted compared to the experimental data, the unsteady pressure coefficient changes that result from leading edge camberline changes can be used to show how an airfoil subjected to these operating conditions can be modified for flutter stability.

The predicted unsteady pressure coefficients for the three different grid sizes are close in agreement with each other, but a larger deviation in the real part is exhibited on each surface for the 301×121 grid. However, the imaginary part of the unsteady pressure coefficient, which governs the work impulse shows much better correlation. Hence, the solutions for the different grid sizes where considered as being in close enough agreement to proceed.

These results do indicate that further work in turbulence and transition modeling for these types of operating conditions is needed.

4.3.10. Optimal Leading Edge Camber Height Case: Steady Flow for $\overline{\alpha} = 10°$

The optimal leading edge camber height case yields stability in the leading edge region with minimum leading edge camber height changes from the baseline airfoil shape while maintaining the baseline airfoil leading edge angle ($\theta = -6.2°$), see Figure 4.35.

The steady flow simulation lift coefficient convergence history is shown in Figure 4.36. The lift coefficient reaches a steady value after the initial transients from the uniform flow initial condition. This indicates the solution has converged.

The change in airfoil shape for the optimal leading edge camber height case generates a change in the steady surface pressure coefficient from the baseline case and the experimental data, as shown in Figure 4.37. There is an increase in the pressure coefficient on each surface in the leading edge region and a decrease in the pressure coefficient in the mid-chord region. In addition, there is good correlation between the solutions for the two different grid sizes.

4.3.11. Optimal Leading Edge Camber Height Case: Unsteady Flow $\overline{\alpha} = 10°$

The unsteady moment coefficient for the oscillating airfoil simulation converges to a sinusoidal wave type shape after two oscillation cycles, Figure 4.38. The overall work-per-cycle converges to a constant value after two oscillation cycles as

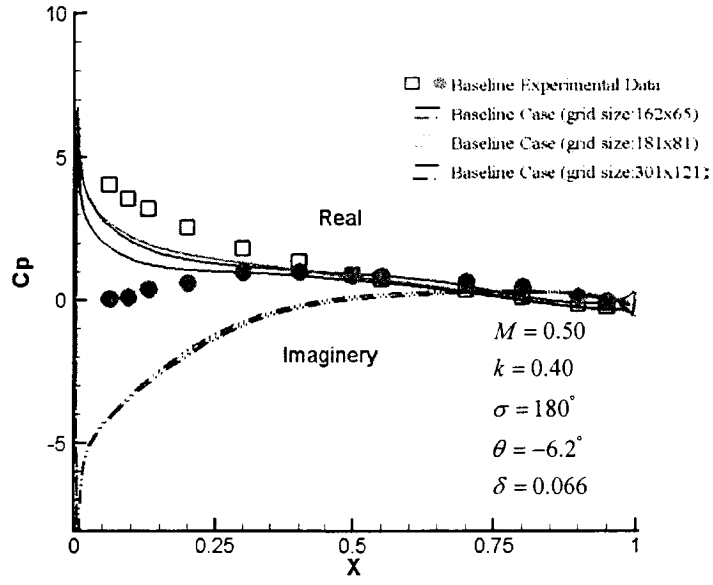

(a) Lower surface

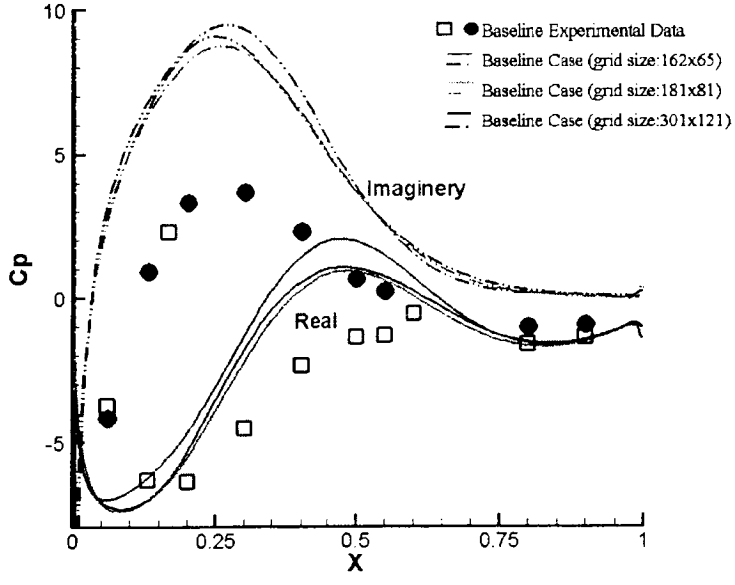

(b) Upper surface

Figure 4.34: High incidence baseline case □rst harmonic unsteady surface pressure coefficient distribution.

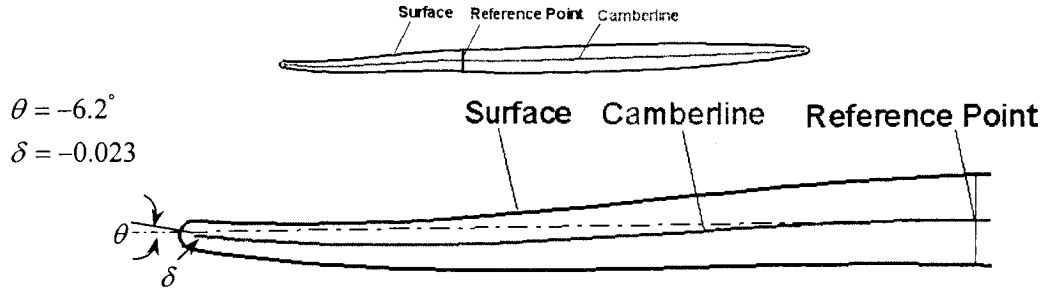

Figure 4.35: Airfoil shape for the optimal leading edge camber height case.

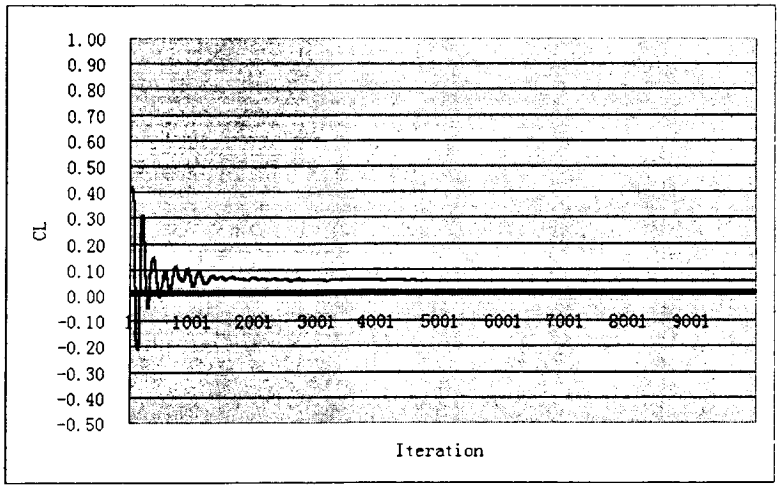

Figure 4.36: Lift coefficient convergence history for the high incidence optimal leading edge camber height case, $\delta = -0.023$.

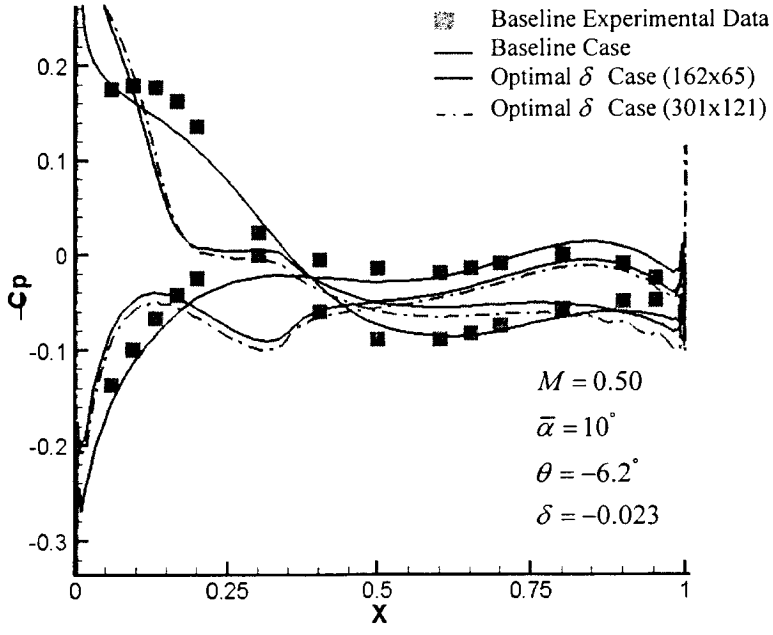

Figure 4.37: Steady surface pressure coefficient distribution for the high incidence optimal leading edge camber height case, $\delta = -0.023$.

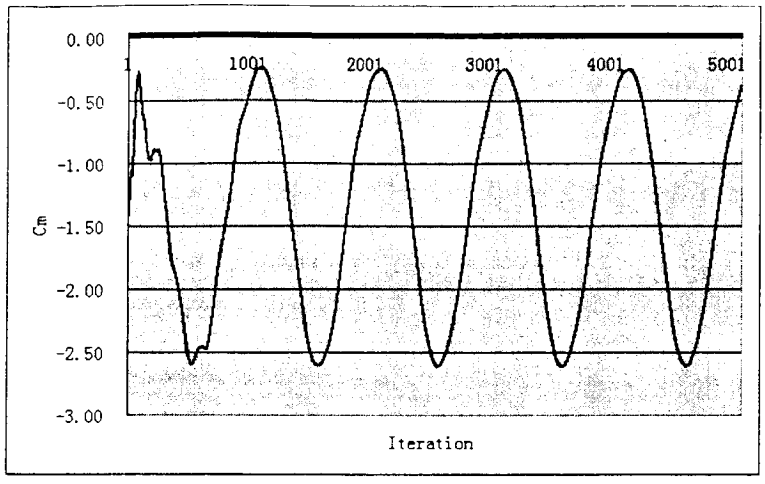

Figure 4.38: Time-dependent moment coefficient for the high incidence optimal leading edge camber height case, $\delta = -0.023$.

illustrated in Figure 4.39. These results indicate the solution has converged to a steady oscillatory solution.

The influence of the change in airfoil shape for the optimal leading edge camber height case on the first harmonic unsteady surface pressure coefficient is depicted in Figure 4.40. The predicted unsteady surface pressure coefficient is increased in value compared to the baseline case over the first half of the airfoil on the lower surface On the upper surface the peak value of imaginary part of the unsteady pressure coefficient is reduced in value and shifted towards the leading edge. The real part has decreased in value aft of 50% chord. Furthermore, there is excellent agreement in the unsteady surface pressure coefficient between the solutions for the two different grid sizes.

From the work impulse results presented in Figure 4.41, the optimal leading edge camber height case indicates stability in the leading edge region. Hence, the optimal leading edge camber height case has been stabilized with a minimum change in δ with constant θ. In addition, there is excellent correlation between the solutions for the two different grid sizes.

Figure 4.42, shows that the flow separates at 0.5% chord; and reattaches at 19.9% chord for the 162×65 size grid and 23.7% chord for the 301×121 size grid. Thus, the separation region has been reduce compared with the baseline case

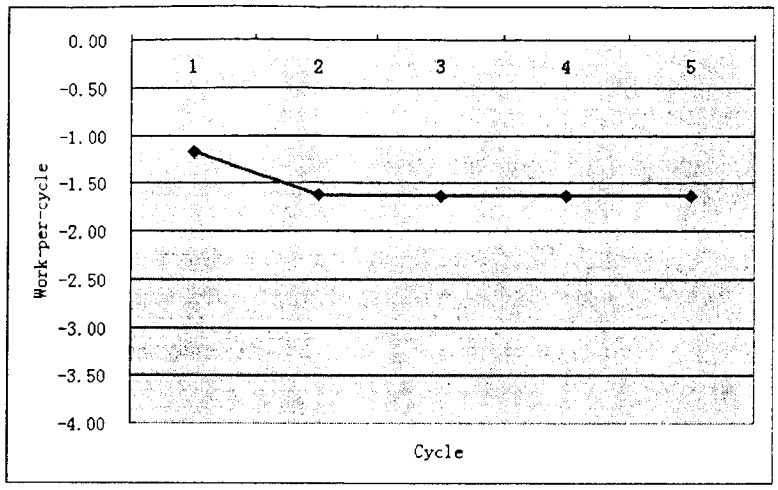

Figure 4.39: Work-per-cycle for the high incidence optimal leading edge camber height case, $\delta = -0.023$.

where the reattachment point was predicted to be at 50% chord for the 181×81 grid and the 301×121 grid.

This approach was also attempted for the leading edge camber angle changes to the NASA/P&W airfoil; i.e. look for a minimal change in θ holding δ constant. Solutions were found for increasing and decreasing values of the leading edge camber angle, θ. There was a concern that these results were being in□uenced to a high degree by the turbulence model and that these solutions needed further investigation.

4.3.12. $\theta = 0°$ and $\delta = 0$ Case: Steady Flow for $\overline{\alpha} = 10°$

The $\theta = 0°$ and $\delta = 0$ airfoil gives a stable work impulse function with both leading edge camber height changes and leading edge camber angle changes. The airfoil shape is shown in Figure 4.22. The lift coefficient convergence history is shown in Figure 4.43. These results indicate the steady □ow solution has converged.

Figure 4.44 shows there is an obvious change in the steady surface pressure coefficient for the $\theta = 0°$ and $\delta = 0$ airfoil compared to the experimental data and the baseline case. The $\overline{C}_p$ is increased in the leading edge region for the both pressure and suction surfaces and decreases along the chord compared with

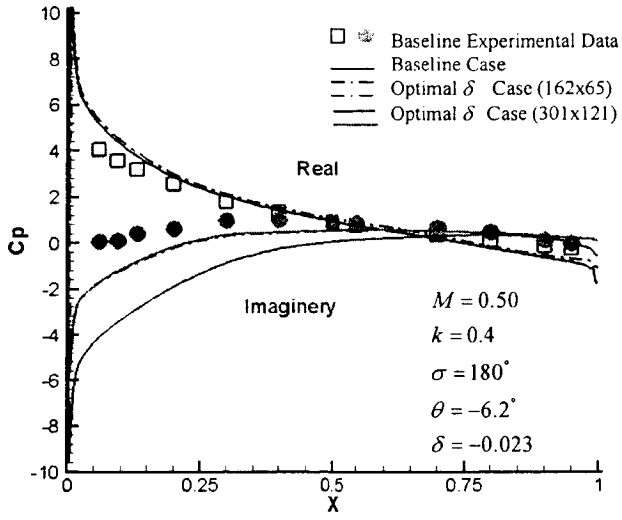

(a) Lower surface

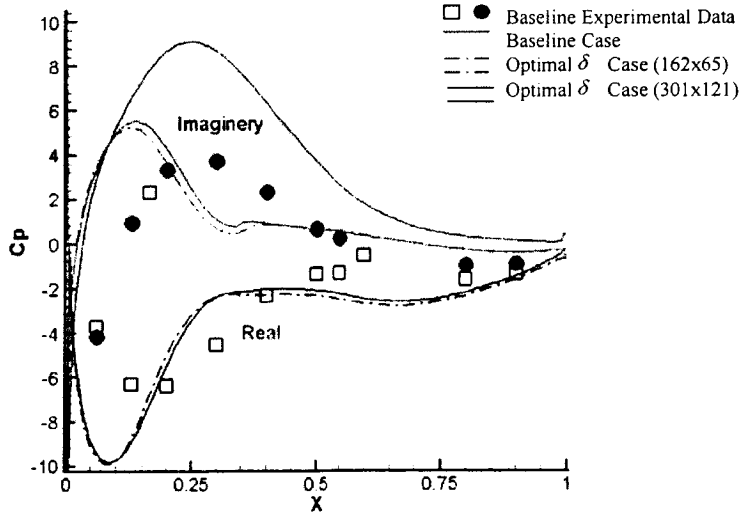

(b) Upper surface

Figure 4.40: First harmonic surface pressure coefficient distribution for the high incidence optimal leading edge camber height case, $\delta = -0.023$.

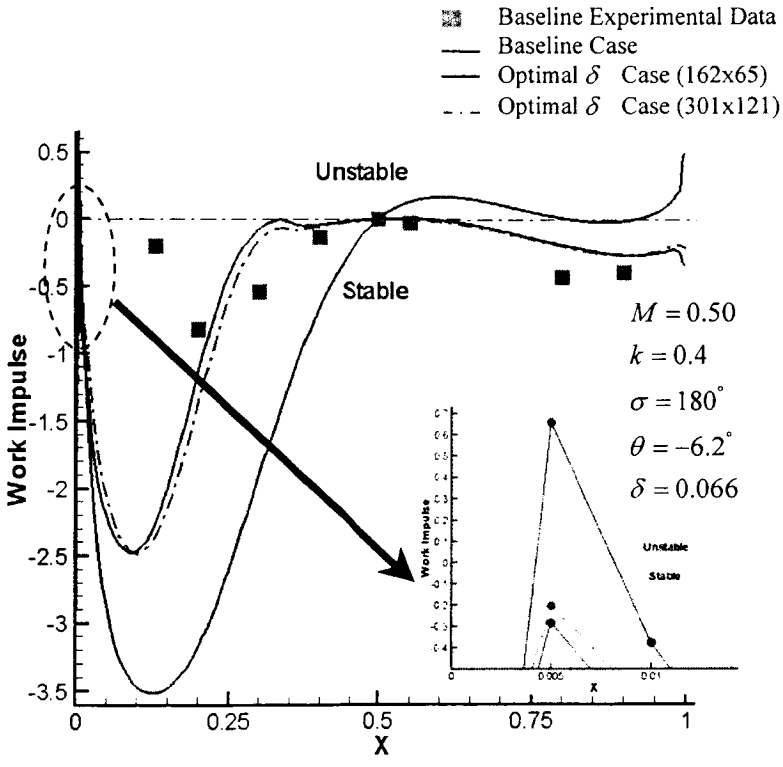

Figure 4.41: Work impulse for high incidence optimal leading edge camber height case, $\delta = -0.023$.

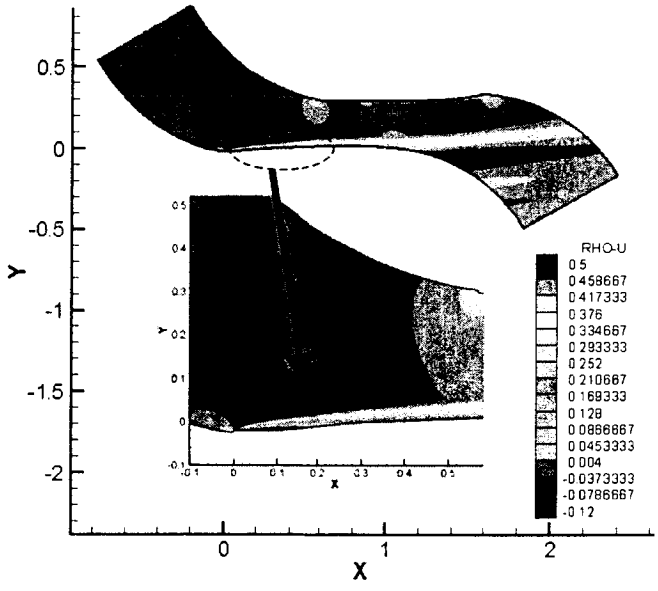

(a) Grid size: 301x121

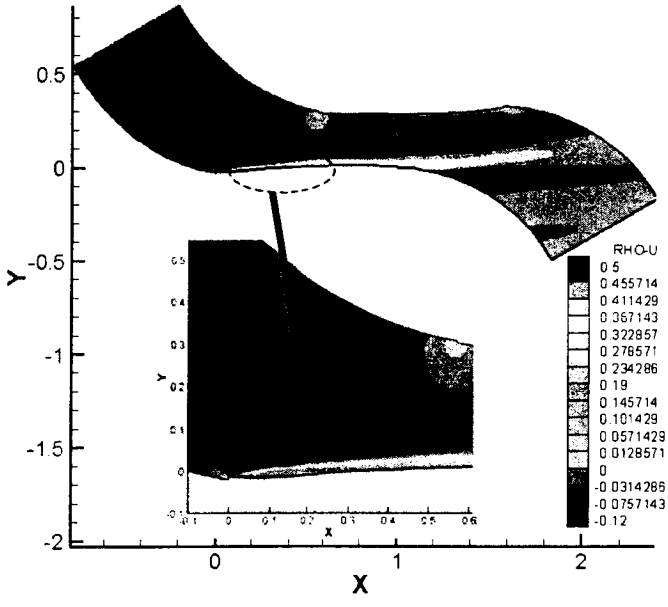

(b) Grid size: 162x65

Figure 4.42: High incidence optimal leading edge camber height case ρu contours.

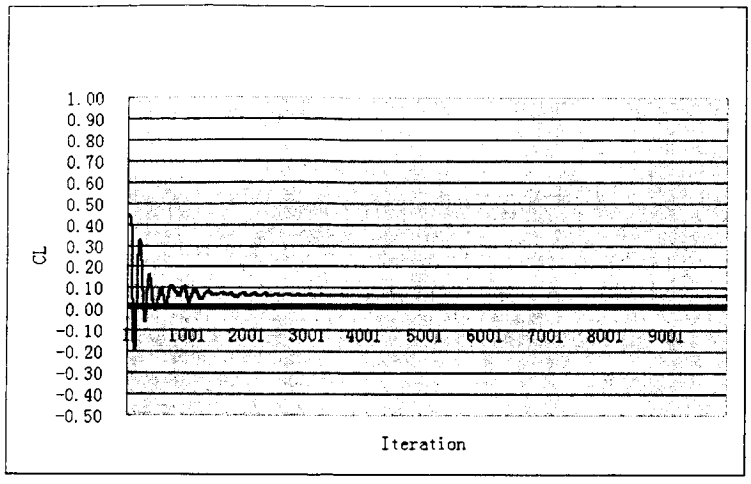

Figure 4.43: Lift coefficient convergence history for the high incidence $\theta = 0°$ and $\delta = 0$ case.

baseline case. The two different grid sizes show good correlation with each other.

4.3.13. $\theta = 0°$ and $\delta = 0$ Case: Unsteady Flow for $\overline{\alpha} = 10°$

For the oscillating airfoil simulation, Figure 4.45 shows the unsteady moment coefficient converges to a sinusoidal type shape in two oscillation cycle indicating a converged solution. This is further illustrated by the work-per-cycle presented in Figure 4.46, which converges to a cycle independent value after two oscillation cycles.

Figure 4.47 illustrates the difference between the baseline case and the $\theta = 0°$ and $\delta = 0$ case for unsteady surface pressure coefficient. As was found in the previous case, the predicted unsteady surface pressure coefficient has increased in value compared to the baseline case over the □rst half of the airfoil on the lower surface On the upper surface the peak value of imaginary part of the unsteady pressure coefficient is reduced in value and shifted towards the leading edge. Also, the real part has decreased in value aft of 50% chord. Excellent agreement is exhibited in the unsteady surface pressure coefficient predictions for the solutions from the two different sized grids.

The work impulse shown in Figure 4.48 indicates the $\theta = 0°$ and $\delta = 0$ case is stable in the leading edge region. As depicted in Figure 4.49, the □ow separation

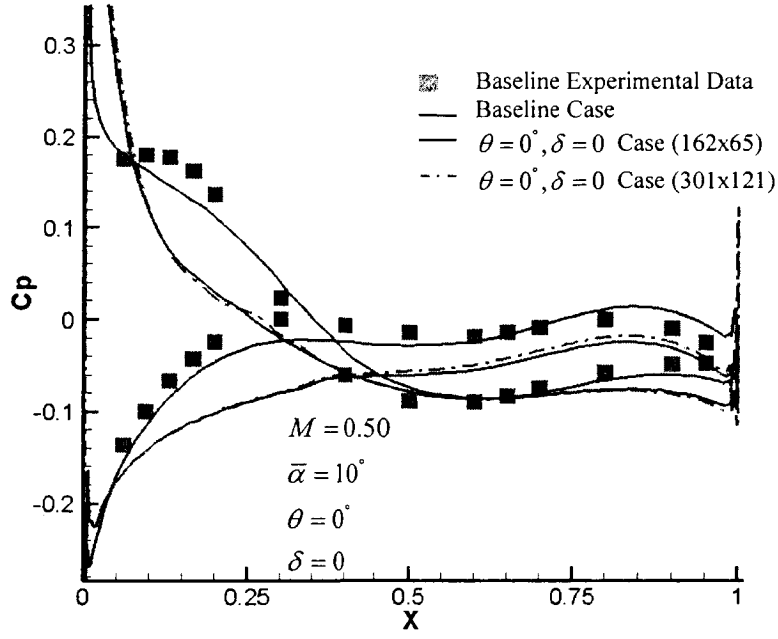

Figure 4.44: Steady surface pressure coefficient distribution for the large mean incidence $\theta = 0°$ and $\delta = 0$ airfoil.

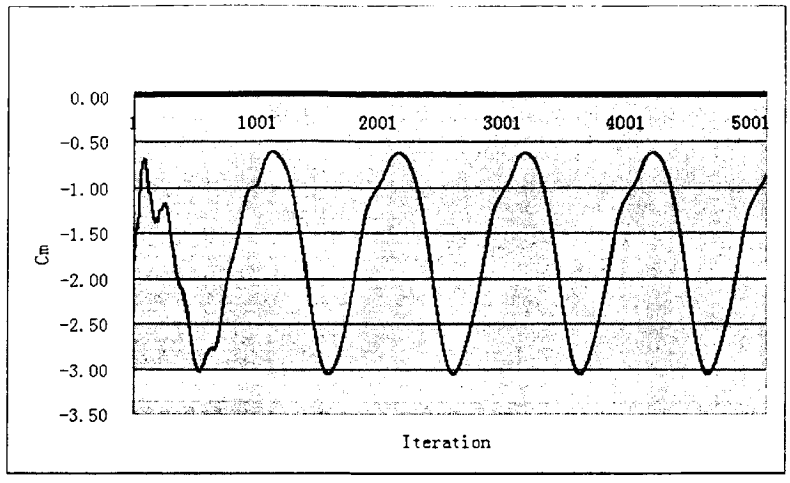

Figure 4.45: Time-dependent moment coefficient for the large mean incidence $\theta = 0°$ and $\delta = 0$ case.

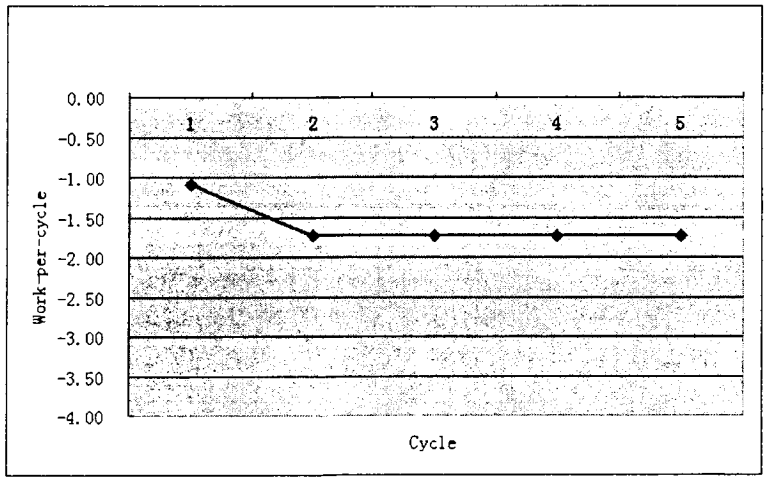

Figure 4.46: Work-per-cycle for the large mean incidence $\theta = 0°$ and $\delta = 0$ case.

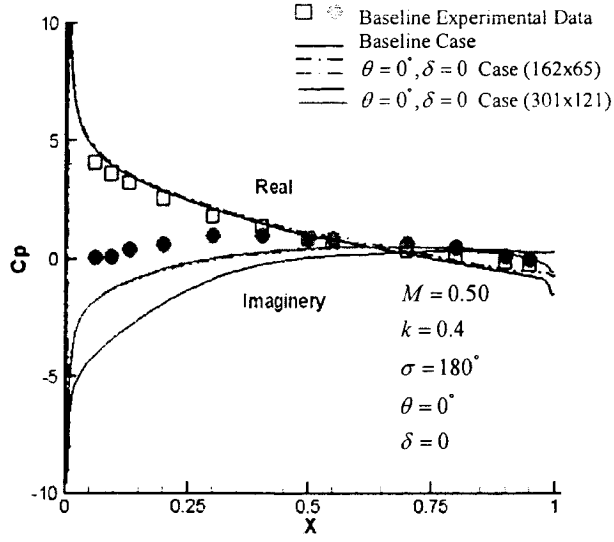

(a) Lower surface

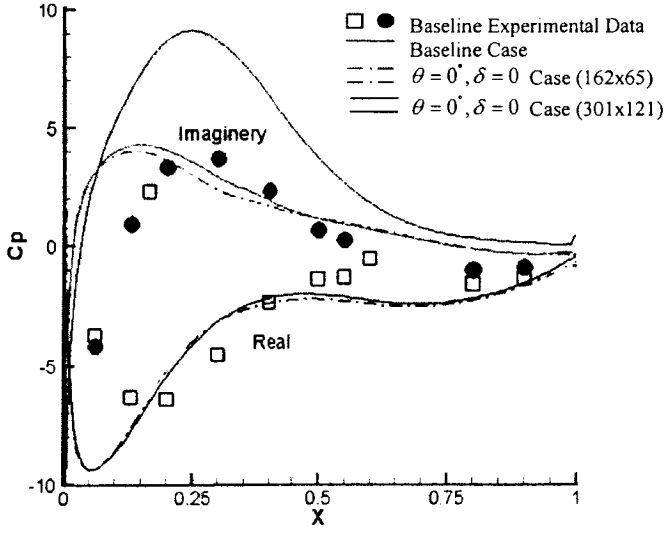

(b) Upper surface

Figure 4.47: First harmonic unsteady surface pressure coefficient distribution for the large mean incidence $\theta = 0°$ and $\delta = 0$ case.

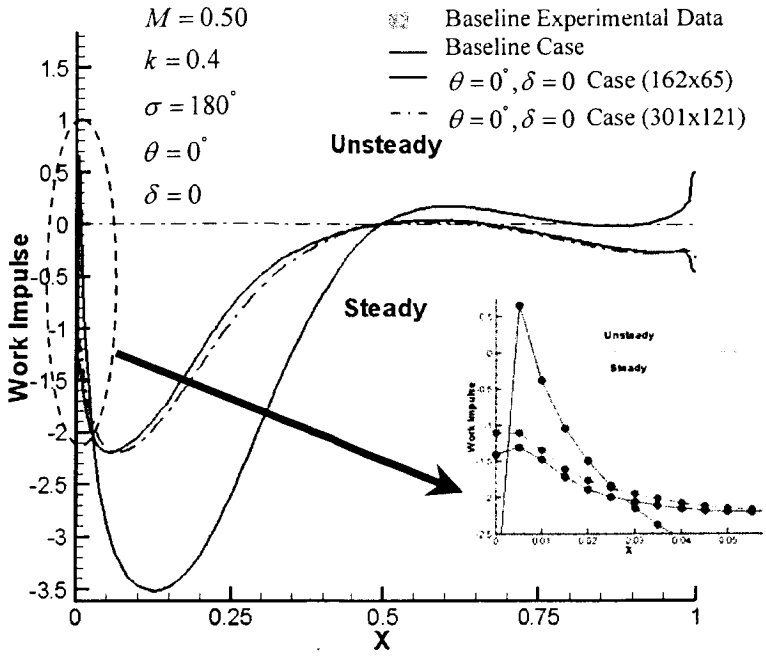

Figure 4.48: Work impulse for the large mean incidence $\theta = 0°$ and $\delta = 0$ case.

point is at 0.5% of chord and the □ow reattachment point is at 22.1% chord for the 162 x 65 grid size, and 20.1% chord for the 301 x 121 grid size. Compared with the baseline case where the reattachment point was predicted to be at 50% chord (181 x 81 and 301 $\times$ 121 grids), the □ow separation region is signi□cantly decreased.

4.4. Summary and Conclusions

In this investigation the in□uence of front camber on □utter of a compressor airfoil was investigated. The airfoil used in this investigation had a cross-section typical of modern high performance low aspect ratio fan or compressor blades in aircraft gas turbine engines. This cross-section would be found near the tip of the blade where the □ow is supersonic at the design point. At part speed operating conditions this portion of the blade would be subjected to high subsonic or transonic Mach numbers and large mean incidence. Viscous effects are of signi□cant impor-

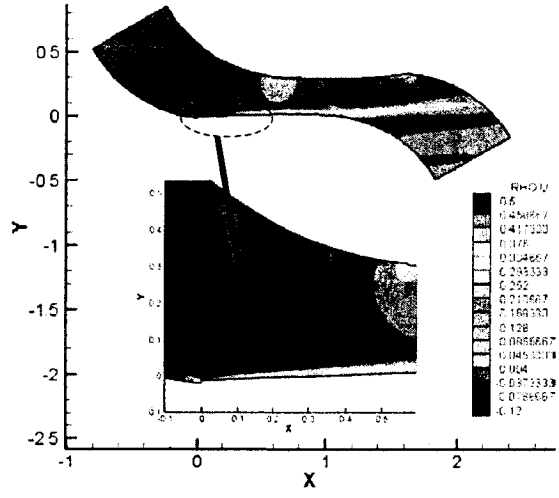

(a) Grid size: 301x121

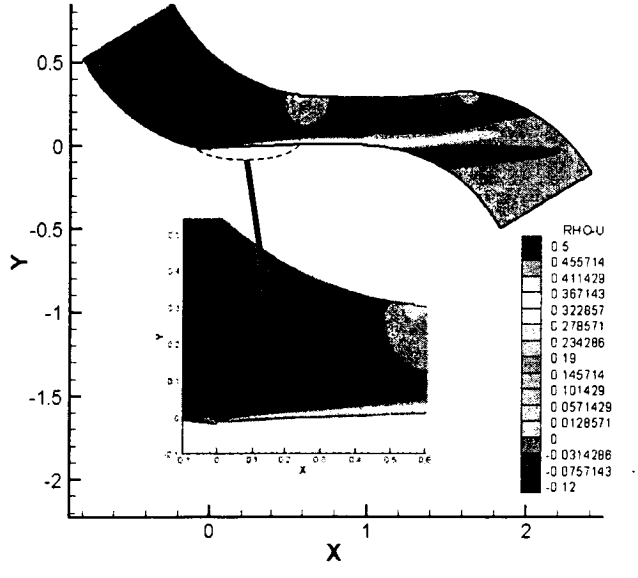

(b) Grid size: 162x62

Figure 4.49: Large mean incidence $\theta = 0°$ and $\delta = 0$ airfoil case ρu contours.

tance at these operating conditions due to flow separation. For these operating conditions the blade would be susceptible to subsonic/transonic stall flutter.

A previous experimental study for this particular airfoil cross-section was conducted in the NASA Transonic Flutter Cascade at the Glenn Research Center. The airfoil design originated at Pratt & Whitney and was given to NASA for testing in the Transonic Flutter Cascade; this airfoil is referred to as the NASA/P&W airfoil. In this investigation it was found that at large mean incidence the flow had a large separation area over the front 40% chord, and in this region there was a contribution towards airfoil instability, i.e. flutter. These results motivated this investigation.

To accomplish the goal of investigating the influence of front camber on airfoil flutter, an airfoil surface coordinate generator was developed. This airfoil surface coordinate generator modified the leading edge region of the original NASA/P&W airfoil by altering the leading edge camberline shape. The leading edge camberline shape was controlled by the leading edge camber height (δ) and the leading edge camber angle (θ), which were modified to change the leading edge airfoil shape. The airfoil camberline shape was represented by a third-order polynomial, and the camberline arc length was constrained to the original value of the NASA/P&W airfoil. The original NASA/P&W airfoil thickness distribution was maintained independent of the camberline shape changes.

The surface coordinate generator, grid generator, and flow solver were combined to find the minimal changes in leading edge shape of the NASA/P&W airfoil to stabilize the leading edge region for flutter.

The flow conditions used in this study were a Reynolds number of 0.9 *Million*, an inlet Mach number of 0.5, chordal incidence angles of 0° and 10°, a reduced frequency of 0.4, and an interblade phase angle of 180°. Both the steady and unsteady flow computational results for the NASA/P&W (baseline) airfoil and a simulated baseline airfoil, which was generated using the NASA/P&W values of δ and θ were compared to validate the geometry generator methodology. The simulated baseline airfoil steady and unsteady flow solutions had good agreement with the baseline airfoil steady and unsteady flow solutions validating the geometry generator.

For the NASA/P&W airfoil contour the steady flow at low mean incidence of ($\overline{\alpha} = 0°$) exhibited good correlation with the experimental data. There was a small area where the predicted steady surface pressure coefficient was larger than the experimental data. This was in the region where a small separation bubble was present. This discrepancy is attributed to the turbulence model and the lack

of a transition model. The unsteady aerodynamic chordwise distribution of the work-per-cycle showed good trendwise correlation with the experimental data, but underpredicted the work contribution in the leading edge region indicating more stability than the experimental data. A region close to the leading edge was predicted to have a positive work-per-cycle contribution. To examine the influence of front camber the an airfoil shape generated for $\theta = 0°$ and $\delta = 0$ was considered. Steady flow prediction for this modified airfoil showed a decrease of the small area of separated flow and an increase in stability in the leading edge region.

For the chordal incidence angle of 0° the airfoil shape generated with $\theta = 0°$ and $\delta = 0$ was considered. Steady flow prediction for this modified airfoil showed a decrease of a small area of separated flow in the leading edge region and an increase in stability in the leading edge region.

The optimal leading edge camber height case was found for the chordal incidence angle of 10°. Steady and unsteady flow predictions for this case was compared with the NASA/P&W airfoil case. There was a decrease in the predicted separation bubble size and an increase in the predicted stability in the leading edge region.

Also, for the airfoil shape generated with $\theta = 0°$ and $\delta = 0$ was considered at a chordal incidence angle of 10°. Steady flow prediction for this modified airfoil showed a decrease in separated flow in the leading edge region and an increase in stability in the leading edge region.

From this investigation, the following major conclusions are drawn:

1. It was demonstrated that front camberline shape is an important factor for stabilizing the work-per-cycle. By using this method, the airfoil shape in the leading edge region can be modified through changes in the leading edge camber angle, θ, and the leading edge camber height, δ, until the work-per-cycle becomes stable.

2. The application of this airfoil shape modification methodology was to decrease or eliminate the probability of flutter in gas turbine engines in this study. However, this method could also be used to improve compressor performance at off-design conditions.

5. Analysis of Periodic Unsteady Pressure Data

To verify the mathematical assumptions used in unsteady aerodynamic models experimental data is needed. Experiments at positive incidence angles have been conducted, for example, by Carta and St. Hilaire[7],[8], Carta[9], Szechenyi and Finas[29], Szechenyi and Girault[30], Buffum et al.[10], Buffum et al.[11], Lepicovsky et al.[31], and Hayden et al.[32]. These experiments cover a range of incidence angles, reduced frequencies, Mach numbers, and interblade phase angles. In these experiments to simulate flutter the blades are force oscillated in a prescribed motion using mechanical or electromechanical mechanisms.

This chapter discusses the analysis of this type of experimental data. The analysis presented accounts for variations that may occur in the forced oscillation system using a spectral block averaging technique. This method (spectral block averaging) subdivides the data into small blocks for analysis, and then averages the results. The results of this method are compared with analyzing the data as a single block. The spectral block averaging method was used in Lepicovsky et al.[33], because of its versatility. This data is used to highlight the difficulties that can occur when analyzing this type of data using a single block approach. Finally, for completeness an analysis that ensemble averages the time-dependent pressure over one cycle of oscillation is considered. It should be emphasized that these procedures can be applied to other time-dependent flow properties.

These analyses were developed to support experiments that were being conducted in the NASA Glenn Research Center Transonic Flutter Cascade (TFC).

5.1. NASA Glenn Research Center Transonic Flutter Cascade

The NASA TFC (Figure 5.1) combined a linear cascade wind tunnel (Figure 5.2) capable of inlet flow approaching a Mach number of 1.2 with a high-speed airfoil

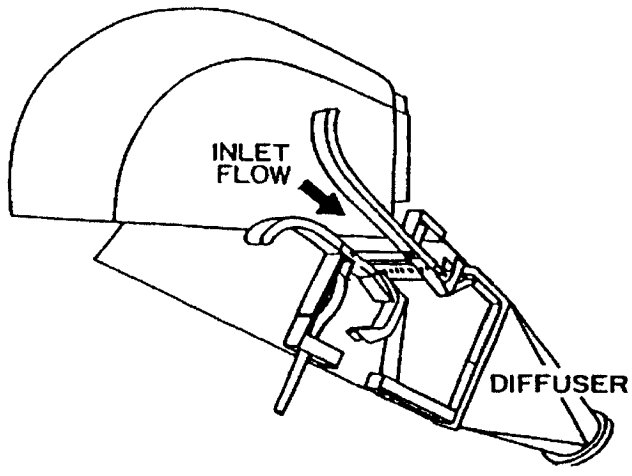

Figure 5.1: Schematic diagram of NASA TFC.

drive system. The drive system produced a torsional (pitching) oscillation to the cascaded airfoils at speci□ed interblade phase angles and realistic values of the reduced frequency. This mechanism may drive from one airfoil up to all nine airfoils. Using different cams the airfoils may be oscillated at amplitudes of 0.6°, 1.2°, or 2.4°.

The airfoil oscillation system is driven by a 74.6 kW electric motor that force oscillates the airfoil in a pitching (torsional) motion. The airfoil motion is generated using a six-cycle sinusoidal groove that is machined in the periphery of nine cams, which can be connected to each individual airfoil through a linkage assembly. Each revolution of the cam gives six oscillations of the airfoil. A proximity probe quanti□es the oscillation motion, Figure 5.3. Due to □uctuations in the motor rotational speed minor □uctuations can be generated in the frequency of oscillation of the blade. Further details on the capabilities of this facility can be found in Buffum and Fleeter[34].

Four airfoils are instrumented with □ush mounted high frequency response pressure transducers to measure the time-dependent pressure during airfoil oscillation. Two airfoils have suction surface instrumentation and two airfoils have pressure surface instrumentation (Lepicovsky et al.[35]). A wall probe with □ve high frequency response pressure transducers can be □ush mounted with the test

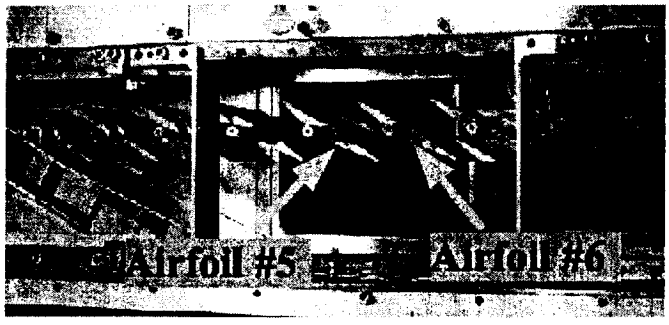

Figure 5.2: Side view of NASA TFC test section.

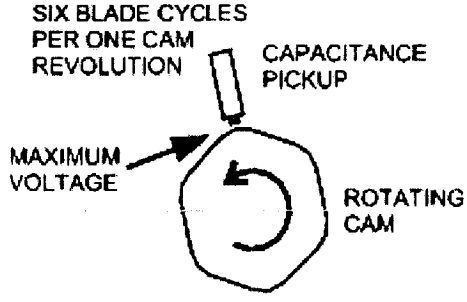

Figure 5.3: Schematic diagram of proximity probe used for the NASA TFC.

section wall (Lepicovsky et al.[33]). This allows unsteady pressure measurements to be taken without the blades present.

5.2. Data Analysis

Typically, the data of interest is the unsteady pressure at the oscillation frequency. To determine the unsteady pressure at the oscillation frequency Fourier transforms are generally used. For unsteady pressure data analysis one obstacle to overcome is that of frequency leakage when using the Fourier transform. There are two types of frequency leakage that will be considered in this paper: typical spectral leakage such as that addressed by Burgess[36], and oscillating frequency leakage that is caused by a slight change in the oscillation frequency of the airfoils. First, some background information about the Fourier Transform is given and then various methods for overcoming these leakage phenomena will be presented.

5.2.1. Fourier Transform

The Fourier transform is a product of the Fourier Series, which allows any signal to be expressed as the sum of sinusoids as shown in Equations 5.1 and 5.2 from Burgess[36]. The transform allows functions to be transformed from the time to the frequency domain allowing each frequency component to be determined.

$$x(t) = \int_{-\infty}^{\infty} X(f)\, e^{i2\pi ft} df, \qquad -\infty < t < \infty \tag{5.1}$$

$$X(f) = \int_{-\infty}^{\infty} x(t)\, e^{-i2\pi ft} dt, \qquad -\infty < f < \infty \tag{5.2}$$

When considering digitally sampled data, the Discrete Fourier Transform (DFT) is used, as shown in Equations 5.3 and 5.4 from Burgess[36].

$$x_k = \sum_{\upsilon=-n/2}^{n/2-1} X_\upsilon e^{i2\pi\upsilon k/n} \qquad 0 \le k \le n-1 \tag{5.3}$$

$$X_\upsilon = \frac{1}{n} \sum_{k=0}^{n-1} x_k e^{-i2\pi\upsilon k/n} \qquad -\frac{n}{2} \le \upsilon \le \frac{n}{2} - 1 \tag{5.4}$$

This leads to the Fast Fourier Transform (FFT), which is used in many numerical applications. The FFT cuts down the computation time from the DFT. A

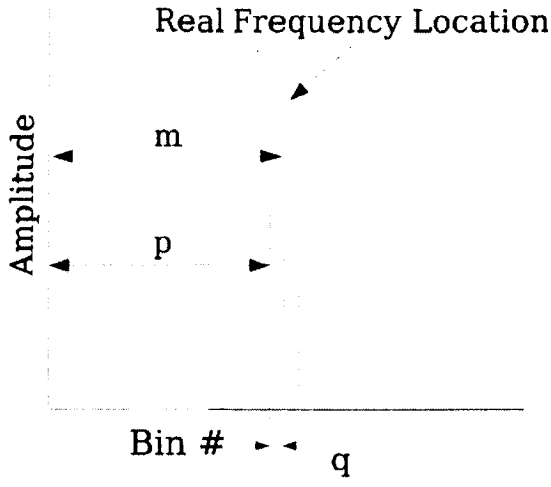

Figure 5.4: Illustration of Burgess nomenclature.

key assumption is the Fourier Transform assumes that the input signal is periodic. When dealing with experimentally acquired data the entire data set may or may not be periodic.

There are other issues to consider when using the Fourier transform. Fourier transforms have some limitations such as the Nyquist criterion that states only frequencies less than half of the sampling rate may be resolved in a Fourier spectrum. For example, in this experiment the sampling rate is $38,000\ Hz$. Therefore, the highest frequency that the Fourier transform can resolve is $19,000\ Hz$. This also leads to an effect called aliasing.

5.2.2. Fourier Transform Leakage Correction

Spectral leakage is caused when the actual frequency does not fall on a data point or bin in the spectrum, see Figure 5.4 as presented by Burgess[36]. Therefore, the amplitude information can be split across more than one bin. Following the method outlined by Burgess, which is repeated below for completeness, the frequency, amplitude, and phase can be corrected.

To start a ratio, Equation 5.5, is de□ned using the complex amplitudes that

straddle the actual frequency. The ratio is constructed so the actual frequency is located closer to the larger amplitude peak in the spectrum. This can be seen by looking at the equation for the non-integer part of the corrected frequency value, Equation 5.6. The integer part of the actual frequency, p, must be selected, by first finding the dominant peak and then examining the adjacent peaks for the largest amplitude. The adjacent peak with the largest amplitude along with the dominant peak make up the correction pair. Since both p and q are always positive, p is always the peak in the correction pair with the lowest bin number.

$$R_q = \frac{|X_p|}{|X_{p+1}|} \tag{5.5}$$

$$q \simeq \frac{1}{1 + R_q} \tag{5.6}$$

The amplitude correction then becomes

$$A \simeq \frac{2\,|X_p|\,\pi q}{\sin(\pi q)} \tag{5.7}$$

or if $|X_{p+1}| > |X_p|$

$$A \simeq \frac{2\,|X_{p+1}|\,\pi\,(1-q)}{\sin(\pi q)}. \tag{5.8}$$

Likewise the frequency correction is

$$f_m \simeq \frac{(p+q)}{T}. \tag{5.9}$$

It is important to note that this correction is for spectral leakage, this method does not address oscillating frequency variation leakage.

5.2.3. Spectral Block Averaging

Spectral block averaging subdivides the time-dependent data - in this case pressure data - into smaller sections or blocks. This is accomplished in the present application of the method by determining the time required to complete multiple cam revolutions, which is determined using the proximity probe. Each revolution of the cam results in six airfoil oscillations. The time-dependent pressure in each block is Fourier decomposed and the first harmonic pressure determined. The first harmonic pressure is then averaged to determine the resultant first harmonic

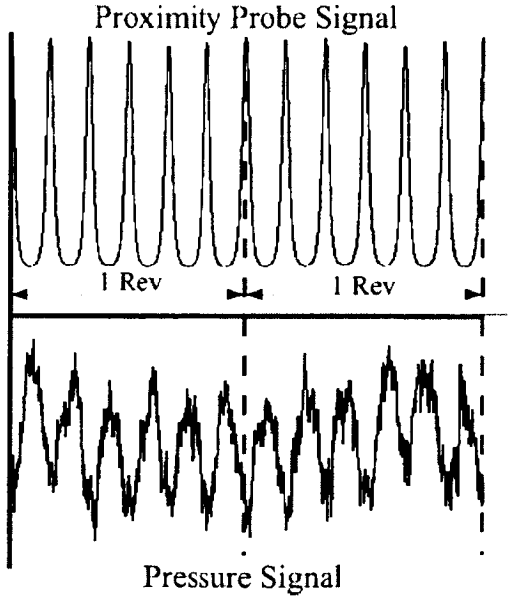

Figure 5.5: Illustration of data blocks.

pressure for the pressure signal. This is a form of the signal enhancement concept discussed by Gostelow[37]. Previous work in this facility, for example Buffum and Fleeter[34] and Buffum et al.[11][10], used a similar technique. However, the blocks of data were de□ned based on 2^n points per block. The equipment used in these previous studies was updated as discussed in Lepicovsky et al.[35]. In addition, the data analysis routines from the previous studies were not available. This motivated the development of the data analysis procedures discussed in this Chapter. Furthermore, the availability of current commercial software allowed more versatility in the data analysis procedures.

The spectral block averaging method is governed by the use of a proximity probe to track the blade motion. The proximity probe signal is used to subdivide the pressure signal into smaller, more manageable pieces or blocks, Figure 5.5.

The smaller blocks of data use a smaller time segment of the periodic signal for analysis. The use of the smaller data blocks allows a more accurate method to account for oscillating frequency variation. Spectral leakage can also be addressed when using this method by leakage correcting each block of data. Each block is then analyzed individually. Once all the blocks have been processed the key

unknowns (pressure frequency, pressure amplitude, phase angle, surface pressure coefficient, etc.) are then averaged. It is important to note that the small changes in the oscillation frequency do not affect the physics of the experiment; it just makes it difficult to perform the Fourier transform accurately.

5.2.4. Ensemble Averaging of the Time-Dependent Signal

A popular method for averaging time-dependent data is the ensemble averaging technique. In the present application of this technique the pressure signal is averaged over one period. This can be challenging since the oscillation frequency is not constant over the entire data set. Actually the frequency can change from one period to the next, changing the number of data points per period and the time it takes to complete one period. Therefore, a mapping scheme is implemented, mapping each point in every period from 0° - 360°. The signal must then be interpolated for all of the individual periods to have the same number of points; this can not be neglected since the oscillation frequency can be changing from one period to the next. All of the individual periods can then be summed and divided by the number of periods to find one ensemble averaged period.

A difficulty that arises with the above procedure is that the time differential between each of the data points (Δt) has been altered by the averaging process. This needs to be accounted for if it is desired to use the Fourier transform on the ensemble averaged results. It was found that using an average (Δt) overcame this difficulty. A flow chart for this process is presented in Figure 5.6.

5.3. Acceleration Correction of Oscillating Blade Data

The TFC oscillates the blades in the cascade in a pitching motion to simulate flutter of a fan or compressor blade. To determine the time dependent pressure during blade oscillation, the blades have been instrumented with high frequency response pressure transducers. During controlled oscillation these pressure transducers are subjected to inertial loading due to the motion of the blade and strain loads due to any flexing of the blade. For discussion purposes these contributions will be called 'inertial loading' or 'acceleration loading'. This time dependent loading on the pressure transducer appears as an additional pressure component. Therefore, the pressure measured during blade oscillation has two contributions. One contribution is due to the unsteady pressure caused by blade oscillation. The second component is due to the inertial loading on the transducer caused by oscillation

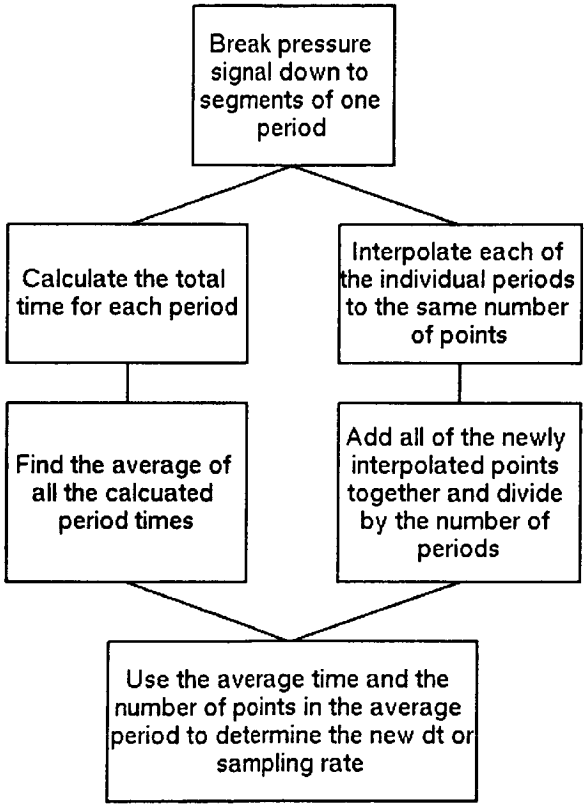

Figure 5.6: Flow chart for ensemble averaging technique.

of the blade in which the transducer is installed. This presents the problem of discerning the unsteady pressure data from the acceleration loading on the pressure transducers. Hence, a correction is needed to account for this additional loading on the transducer.

To correct for the acceleration loading on the transducers a series of experiments were undertaken. In this series of experiments blade oscillations were conducted in the TFC with no flow so that the acceleration loading could be quantified using the same oscillation mechanism that would be utilized during actual testing; it is preferable to conduct these experiments in a vacuum. From these experiments the 'apparent pressure' due to inertial loading is determined for each blade-mounted transducer over the entire range of blade oscillation frequencies that will be used in the flutter simulation experiments. This 'pressure' signal is Fourier decomposed into harmonics and the amplitude and phase are quantified for each frequency of oscillation and for each pressure transducer.

These results represent correction coefficients that are used to modify the unsteady pressure measurements from flutter simulations for acceleration loading. This is accomplished by using the following procedure. The unsteady pressure measurements from a flutter simulation experiment are transformed to the frequency domain using Fourier decomposition (Spectral Block Averaging Analysis). The correction coefficients, which represent the 'apparent' pressure loading due to inertial loading on the pressure transducer, are then subtracted from the measured unsteady pressure. From this operation the unsteady pressure due to blade oscillation is recovered, as given by the following equation.

$$\frac{\text{Corrected Pressure}}{\text{Motion}} = \frac{\text{Pressure}}{\text{Motion}} - \frac{\text{No Flow 'Apparent' Pressure}}{\text{Motion}} \tag{5.10}$$

Figure 5.7 is a flow chart that illustrates the process.

5.4. Results

In this section results are presented for data taken from three series of experiments. The first series concentrated on collecting time-dependent pressure data from a wall probe with the center airfoil oscillating (airfoil *#5*) in the cascade with all other airfoils fixed. In the second series of experiments, time-dependent pressure data was acquired from the blade mounted transducers on a stationary airfoil (airfoil *#6*) adjacent to the center oscillating airfoil. The final series of experiments

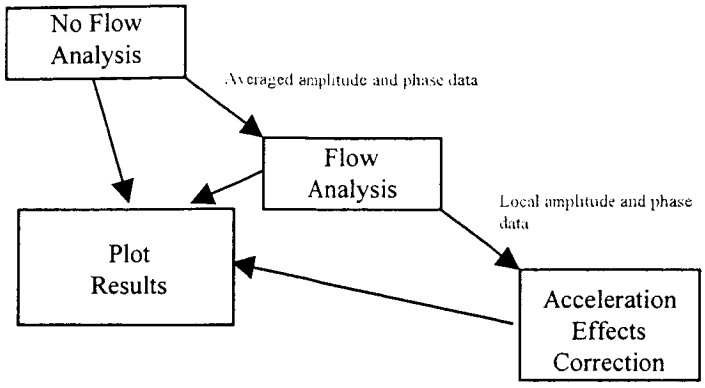

Figure 5.7: Flow chart illustrating the steps necessary to correct for transducer acceleration loading.

involves the measurement of the unsteady pressure from the transducers mounted on the center oscillating airfoil (airfoil *#5*).

In the first and second series of experiments, the center airfoil (airfoil *#5*) was oscillated at frequencies from 200 Hz to 500 Hz, in 100 Hz increments. A comparison is made between the spectral block averaging method and a spectral analysis based on using the entire data set as a single block. The wall probe results are for a cascade inlet Mach number of 0.8, and the airfoil results are for a cascade inlet Mach number of 0.5.

Experiment series three presents both flow, Mach number of 0.5, and no flow results showing the acceleration correction analysis process in detail for one transducer. Results will then be presented for all of the working transducers on the KS2 airfoil for frequencies from 50 Hz to 500 Hz in 50 Hz increments.

5.4.1. Data Analysis

Wall Probe

Figure 5.8 illustrates the change in the first harmonic pressure amplitude at the cascade wall between airfoils *#5* and *#6* as the frequency of the center oscillating airfoil is changed from 200 to 500 Hz.

The spectral block analysis method has slightly increasing amplitude as the oscillation frequency increase. However, conducting the spectral analysis using

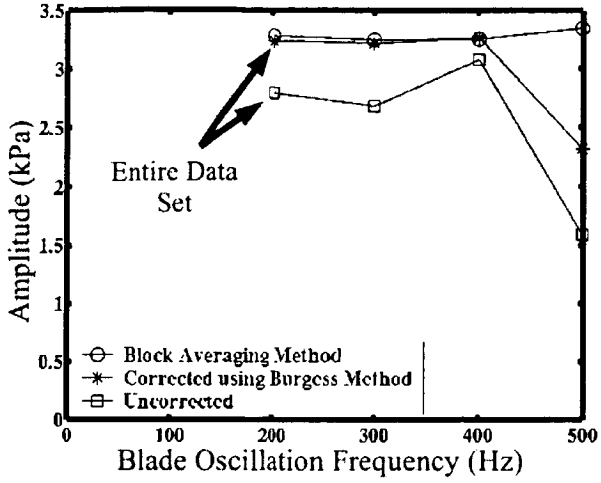

Figure 5.8: Comparison of the spectral block averaging and typical FFT method using time-dependent pressure data taken from the wall probe.

the entire data set resulted in amplitudes that were lower in amplitude than the spectral block averaging technique. This was a result of the classical spectral leakage and the slight variation of the airfoil oscillation frequency over the duration of the experimental data set. Correcting the first harmonic amplitude for spectral leakage using the Burgess method presented above improves the correlation with the spectral block averaging technique except at 500 Hz, which still exhibited a much lower first harmonic amplitude.

Examining the spectrum for 500 Hz it was found that a dominant frequency was not apparent, as shown in Figure 5.9. This indicates that the forced oscillation frequency was fluctuating over the duration of the data set resulting in the oscillation frequency being spread over multiple bins in the spectrum. The relations presented by Burgess are not applicable for this case. The variation in the oscillation frequency for the 400 Hz and 500 Hz data is illustrated in Figure 5.10, which presents the frequency as a function of block number from the spectral block averaging method.

From this figure it can be seen the oscillation frequency variation is larger for 500 Hz than for 400 Hz. While the frequency varies only slightly over the duration of the test, this variation is large enough to have an effect on the Fourier

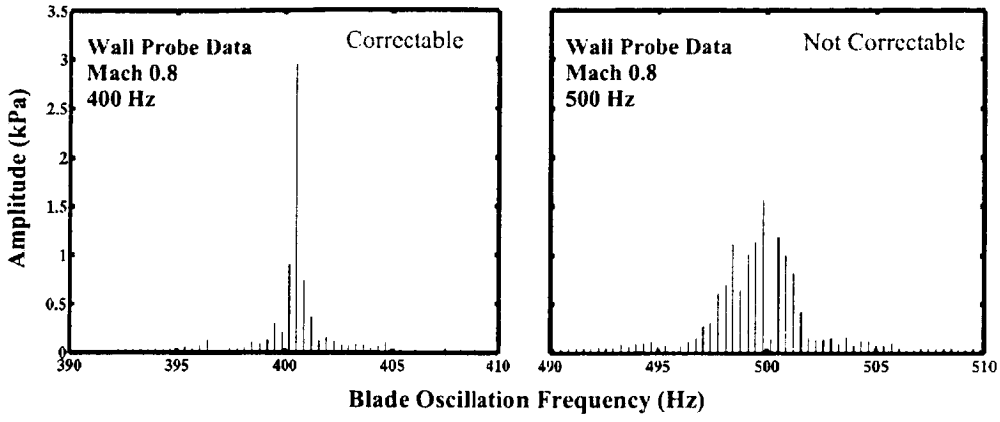

Figure 5.9: Spectra demonstrating different levels of frequency leakage for the wall probe unsteady pressure data.

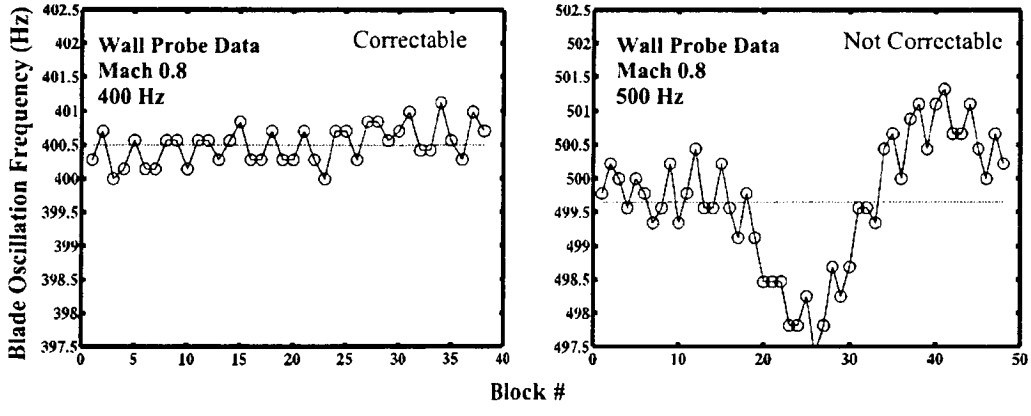

Figure 5.10: Frequncy-per-block results demonstrating the relatively large frequency change for the wall probe due to variations in the center airfoil oscillation frequency.

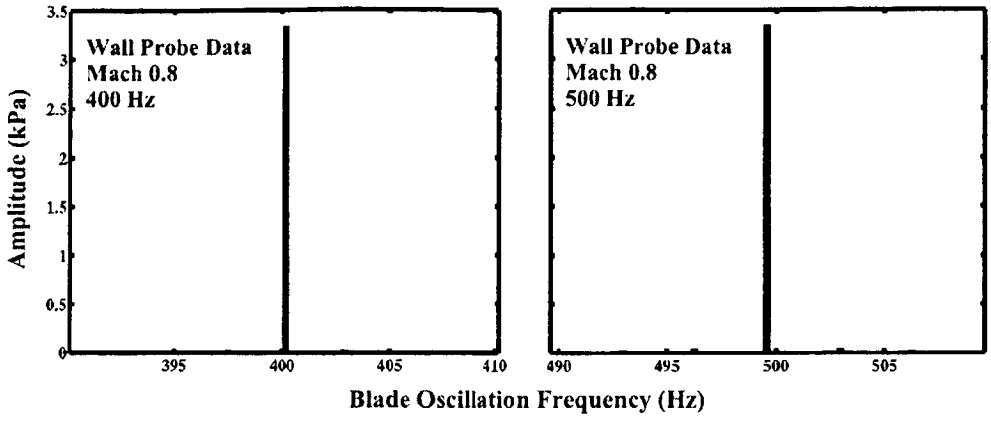

Figure 5.11: Spectra for one data block from the Spectral Block Average method for the wall probe data.

transform.

Spectral block averaging subdivides the data into smaller blocks and uses the proximity probe to insure the data is periodic. This normally provides results where Burgess's leakage correction is not necessary. One block of data for 400 and 500 Hz oscillation frequency is shown in Figure 5.11.

A well de□ned peak can be found at each oscillation frequency with negligible leakage. This illustrates one of the bene□ts of using the spectral block average method.

Stationary Airfoil Adjacent to Oscillating Airfoil

Analogous results are found for the unsteady pressure measured on airfoil $\#6$ adjacent to the oscillating airfoil $\#5$. Figure 5.12 shows the change in the □rst harmonic pressure amplitude as the frequency of the center oscillating airfoil is changed from 200 to 500 Hz.

As was shown above, conducting the spectral analysis on the entire data set results in amplitudes that have a lower amplitude than the spectral block averaging method. Correcting the □rst harmonic amplitude for spectral leakage is seen to improve the correlation with the spectral block averaging technique except at 200 and 500 Hz, which still exhibited a lower □rst harmonic amplitude.

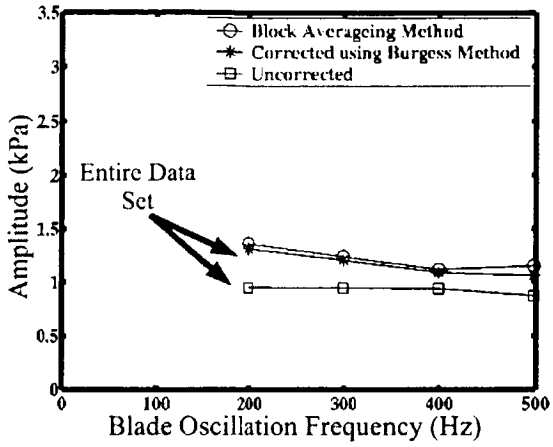

Figure 5.12: Comparison of the specral block averaging and typical FFT method for unsteady pressure data from one transducer on airfoil $\#6$.

This deviation is attributed to the □uctuation of the airfoil oscillation frequency. The variation of the oscillation frequency as a function of block number from the spectral block averaging method is illustrated in Figure 5.13.

The □gure shows that although small the frequency variation is more for 200 Hz than for 300 Hz. Figure 5.14 again shows that each block has a well de□ned peak, eliminating the effects of the slight change in the oscillation frequency.

Ensemble Averaging

For completeness, it was also desirable to compare the spectral block averaging method to the ensemble averaging method. Figure 5.15 shows the time-dependent wall probe pressure ensemble averaged over one period of oscillation of the center airfoil. In this □gure the center airfoil is oscillating at a frequency of 400 Hz. The periodic nature of the data is clearly evident.

Fourier transforms of the ensemble averaged data were conducted using the Δt determined from the averaging process for the data sampling period for each airfoil oscillation frequency. These Fourier transforms are compared with the spectral block averaging method in Figure 5.16. This □gure shows exceptional correlation between the two methods.

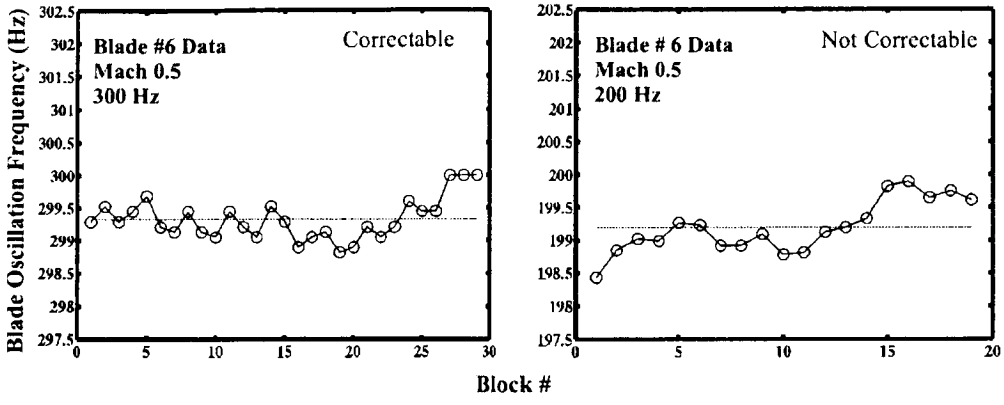

Figure 5.13: Frequency-per-block results demonstrating frequency change for a pressure transducer on airfoil *#6*.

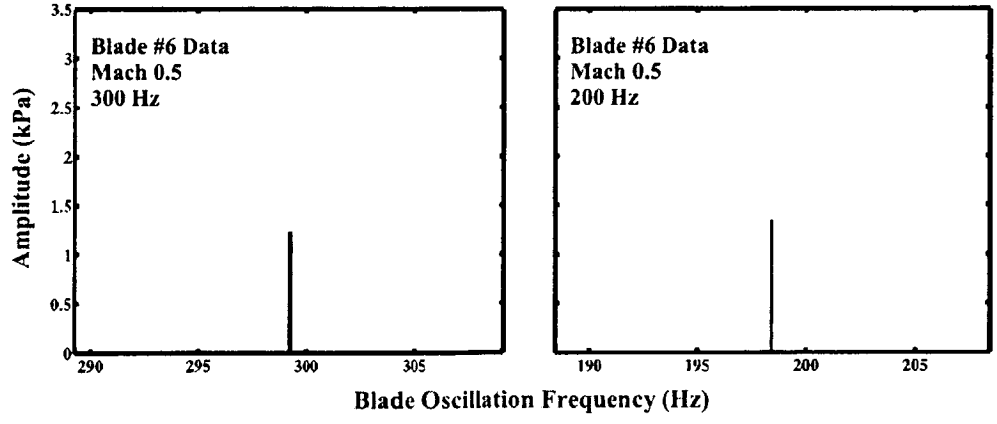

Figure 5.14: Spectra for one data block from the Spectral Block Average Method for a pressure transducer on airfoil *#6*.

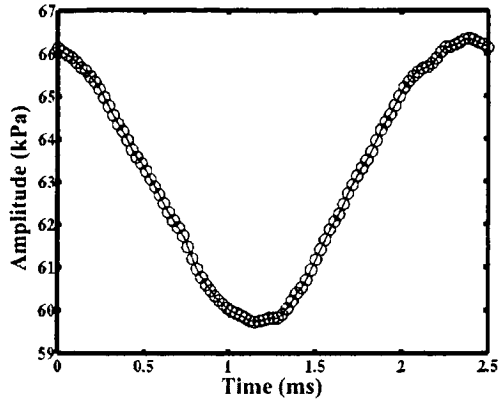

Figure 5.15: Ensemble averaged pressure for wall probe pressure transducer with the center cascade airfoil oscillated at a frequency of 400 Hz.

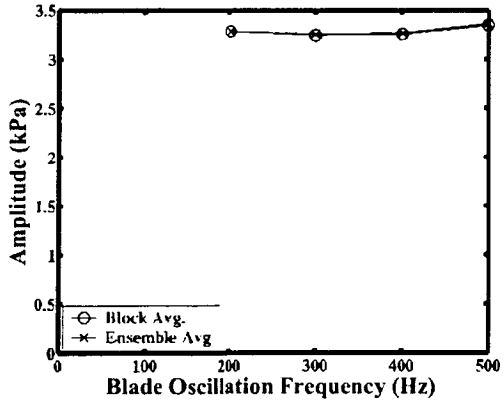

Figure 5.16: Comparison of Spectral Block Averaging and Ensemble Averaging for pressure data from a wall probe transducer with the center cascade airfoil oscillated over a range of frequencies.

5.4.2. Acceleration Correction

The analysis procedure for acceleration correction will be shown in detail for Kulite transducer 11 at an oscillation frequency of 200 Hz. The data set C2_69_05_KS2_11 is for no □ow. The corresponding data set that has a test section Mach number of 0.5 is C2_69_37_KS2_11. Figure 5.17 presents the results of the Fourier analysis performed on these two sets of data.

In each case the data set is analyzed using the spectral block averaging method. Figure 5.17(a) is for the no □ow case and Figure 5.17(b) is for the □ow case. The top most plots in Figures 5.17(a) and 5.17(b) illustrate the variation of the pressure amplitude as a function of block number. Each data block is composed of 5 cam revolutions or 30 oscillation cycles. There is a variation in the pressure amplitude from block-to-block, which is very small for the no □ow case. Note that for the $M = 0.5$ case the pressure signal has not been corrected for acceleration loading. The second plot in each column is the phase angle.

The third plot in each column presents the ensemble averaged signal and the Fourier reconstructed signal using the averaged □rst harmonic signal amplitude and phase. The ensemble averaging was conducted over one cycle of oscillation. The ensemble averaged signal exhibits some high frequency components that are superimposed on the 200 Hz blade oscillation frequency. The Fourier reconstructed signal using the □rst harmonic amplitude and phase from the Spectral Block Averaging technique is seen to be a good representation of the 'mean' of the ensemble-averaged data. The Fourier spectrum of each block of data (fourth plot in each column) illustrates the signal is composed of the □rst harmonic of the blade oscillation frequency with smaller higher order harmonics, plus some much higher frequency contributions.

From the ensemble averaging it is apparent that these high frequency components are synchronous with blade oscillation. If the higher frequency were not in-phase with the blade oscillation, the higher frequency components would have been substantially reduced in magnitude or eliminated by the ensemble averaging process. To examine this further the proximity probe and pressure signal were interrogated; the data from the proximity probe was used to determine the time dependent change in blade angle during oscillation. These signals are presented in Figure 5.18.

Comparing the motion signal to the pressure signal it can be observed that at the +/- peaks of the oscillation motion that there is a rapid increase in the □uctuations of the pressure signal. This occurs at the location where the blade changes from a pitching up motion to a pitching down motion for the positive peak,

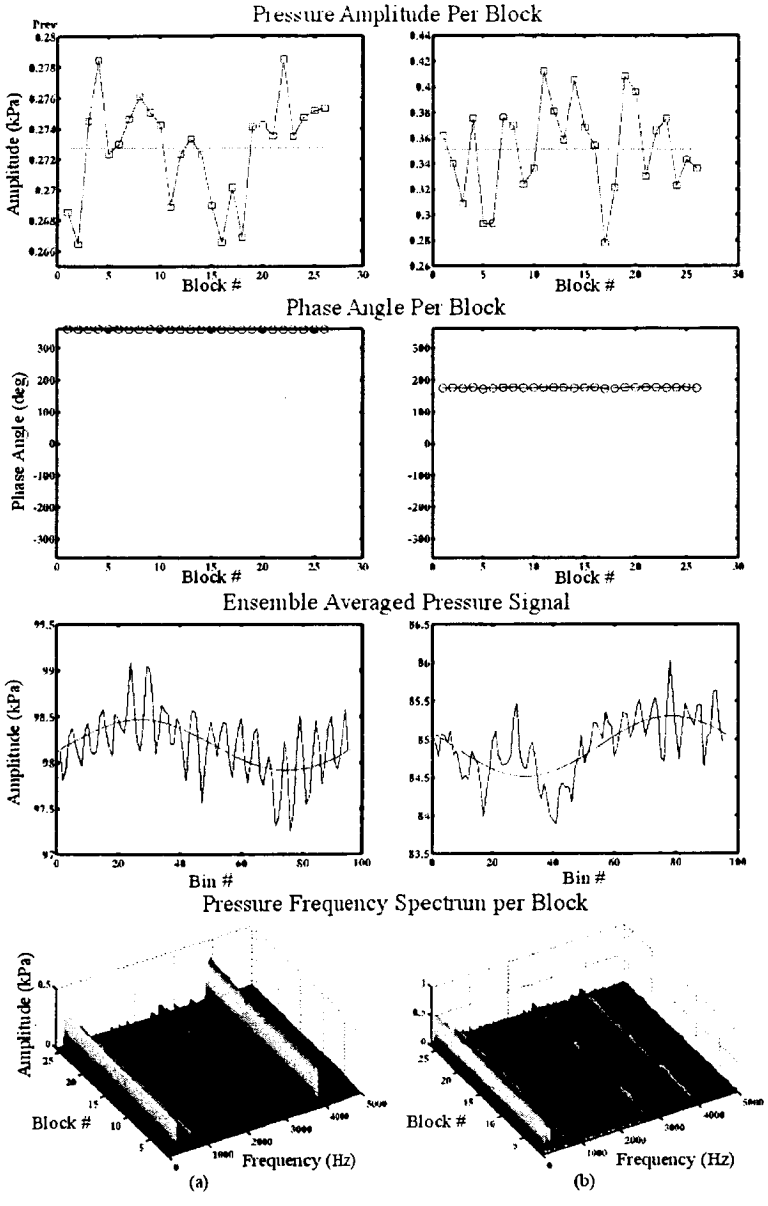

Figure 5.17: Time dependent pressure measurement from Kulite pressure transducer 11 on blade KS2 oscillating at 200 Hz, (a) pressure signal for no flow; and (b) pressure signal with a test section Mach number of 0.5.

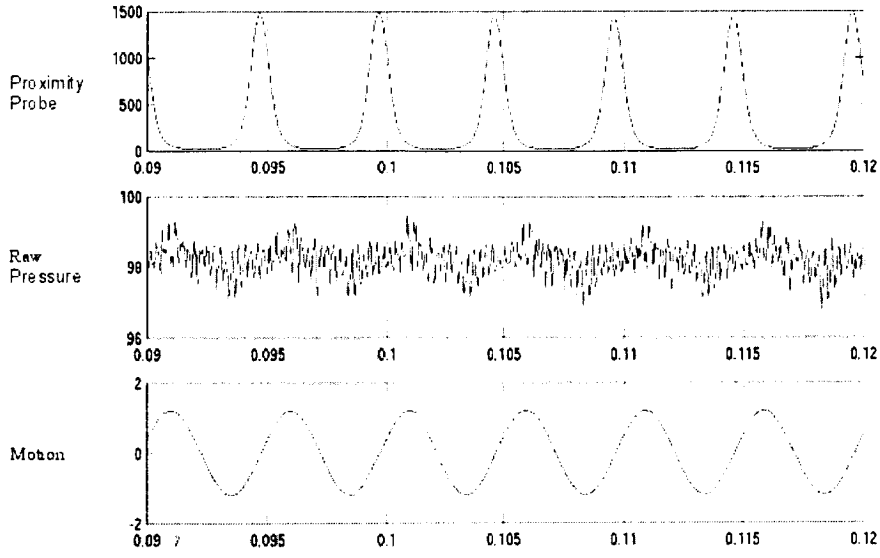

Figure 5.18: Time dependent measurements from the proximity probe and the pressure transducer under no-flow conditions with a blade oscillation frequency of 200 Hz for one cam revolution. The motion signal, which represents the blade oscillation amplitude in degrees, is calculated using the proximity probe measurements.

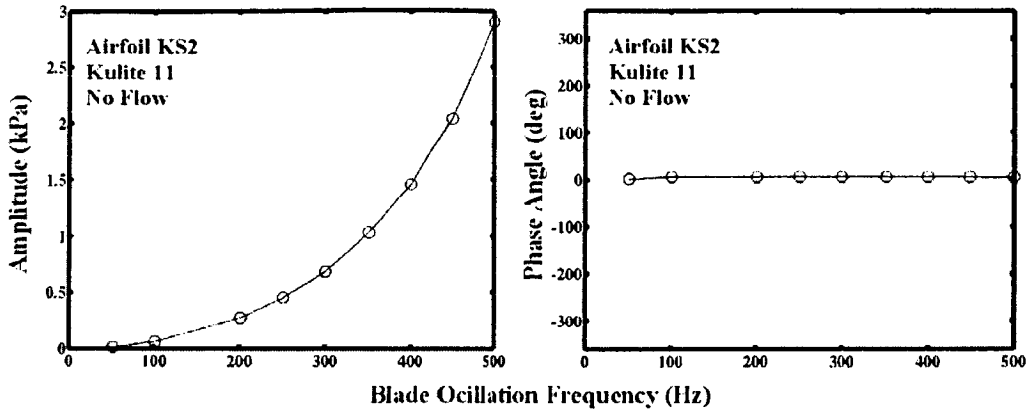

Figure 5.19: Pressure correction amplitude and phase for KS2 pressure transducer 11.

and where the blade changes from a pitching down motion to a pitching up motion for the negative peak. It is possible that the blades are subjected to an impulse load at each of these locations. Hence, the source of the transducer response could be a result of the blade responding at its natural frequencies or possibly a resonant response of the transducer-RTV system; note that the transducers are covered with a thin protective layer of RTV, which is □ush with the airfoil surface. The source of this response needs further investigation.

Using this technique of oscillating the blades for the no-□ow condition, correction coefficients for all blade mounted pressure transducers are quanti□ed. Figure 5.19 illustrates the change in amplitude and phase for transducer 1 on blade KS2 as a function of oscillation frequency.

The amplitude correction is observed to increase quadratically with oscillation frequency. This is to be expected since the acceleration amplitude will increase as the square of the oscillation frequency. Little change in the phase correction factor was found with increasing oscillation frequency. This is typical of the results obtained for all the pressure transducers. Hence, these calibration curves are constructed for each pressure transducer and are used to correct for acceleration loading on the pressure transducers during □utter simulations. Figure 5.20 illustrates the amplitude correction for all pressure transducers on blade KS2 over the range of oscillation frequencies used in the TFC.

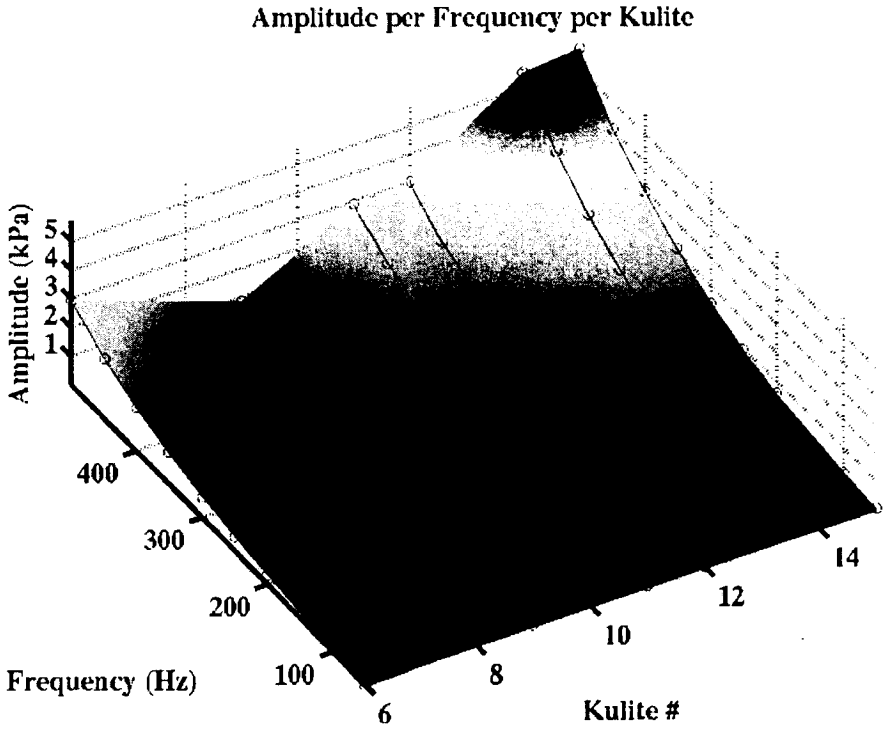

Figure 5.20: Amplitude correction factors for pressure transducers on airfoil KS2.

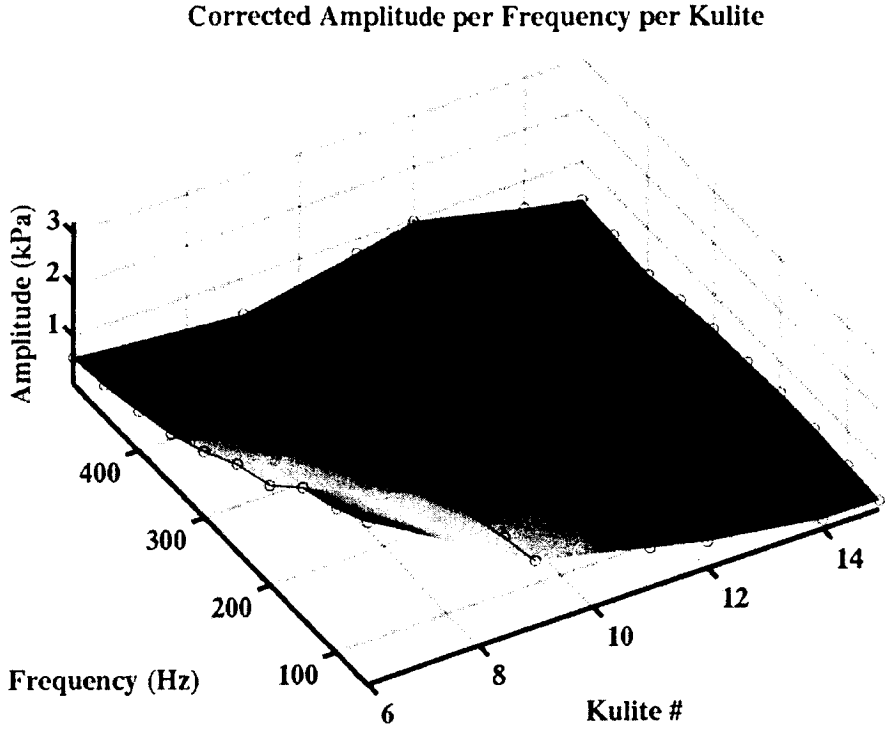

Figure 5.21: Corrected pressure amplitudes for airfoil KS2 at a test section Mach number of 0.5.

Using these calibration curves for the pressure transducers on blade KS2, the experimental data for blade oscillation at a test section Mach number of 0.5 is corrected using Equation 5.10. The results of the correction process are presented in Figure 5.21. This analysis is completed by calculating the acceleration corrected □rst harmonic surface pressure coefficients.

5.5. Summary and Conclusions

This chapter presented a comparison of different data analysis techniques for periodic unsteady data. Analysis results were presented for data generated in the NASA Glenn Research Center Transonic Flutter Cascade. The unsteady pressures

were measured using high frequency response pressure transducers. In each case airfoil #5 was oscillated at incremental frequencies. The application was for time dependent pressures generated from oscillating airfoils. However, the methods could be applied to other time-dependent quantities.

The spectral block averaging method was presented. This method was able to account for variations in the airfoil oscillation frequency because it subdivides the data into small enough blocks that the effects of oscillation frequency change are negligible. This makes the spectral block averaging method more versatile when analyzing unsteady data than the traditional method of performing a Fourier transform on an entire data set.

Ensemble averaging is a common method of processing periodic signals. Like the spectral block average method, ensemble averaging can also account for the changes in oscillation frequency.

Previous data analysis for this research has used the Spectral Block averaging method (Buffum et al.[10] and Buffum and Fleeter[34]). This previous work used a block size based on 2^n and therefore it was not naturally periodic like the analysis presented here. However by using a combination of a small block of pressure data and a leakage correction routine, such as that presented by Burgess, this previous work was successful in accounting for oscillating frequency variation. The equipment used for this research was updated (Lepicovsky et al.[35]) and the data analysis routines were not available. This motivated the development of the data analysis procedures reported in this section. In addition, the availability of current commercial software allowed more versatility in the data analysis procedures.

An correction method was presented for inertial effect on transducers mounted in oscillating airfoils. An analysis of the time dependent pressures from the transducers mounted on the center airfoil during oscillation uncovered some high frequency components. Two possible sources of these frequencies are the airfoil responding at its natural frequencies or a resonant response of the transducer-RTV system. The source of this response needs further investigation.

BIBLIOGRAPHY

[1] Chen, J. P., and W. R. Briley, 2001, "A Parallel Flow Solver for Unsteady Multiple Blade Row Turbomachinery Simulations," ASME Paper 2001-GT-0348.

[2] Weber, S. and Platzer, M.F., 2000, "A Navier-Stokes Analysis of the Stall Flutter Characteristics of the Buffum Cascade", ASME Paper 2000-GT-385.

[3] Swafford, T.W., Loe, D.H., Huff, D.L., Huddleston, D.H., and Reddy, T.S.R., 1994, "The Evolution of NPHASE: Euler/Navier-Stokes Computations of Unsteady Two-Dimensional Cascade Flow Fields," AIAA Paper No. AIAA-94-1834.

[4] Ekaterinaris, J.A. and Platzer, M.F., 1996, "Numerical Investigation of Stall Flutter," ASME Journal of Turbomachinery, Vol. 118, pp. 197-203.

[5] Sidén, L.D.G., 1991, "Numerical Simulation of Unsteady Viscous Compressible Flows Applied to Blade Flutter Analysis," ASME 91-GT-203.

[6] Wu, J., Huff, D.L., and Sankar, L.N., 1989, "Evaluation of Three Turbulence Models for the Prediction of Steady and Unsteady Airloads," NASA Technical Memorandum 101413.

[7] Carta, F.O. and St. Hilaire, A.O., 1978, "Experimentally Determined Stability Parameters of a Subsonic Cascade Oscillating Near Stall", ASME Journal of Engineering for Power, Vol. 100, No. 1, pp. 111-120.

[8] Carta, F.O. and St. Hilaire, A.O., 1980, "Effect of Interblade Phase Angle and Incidence Angle on Cascade Pitching Stability," ASME Journal of Engineering for Power, Vol. 102, No. 2, pp. 391-396.

[9] Carta, F.O., 1983, "Unsteady Aerodynamics and Gapwise Periodicity of Oscillating Cascaded Airfoils," ASME Journal of Engineering for Power, Vol. 105, pp. 565-574.

[10] Buffum, D.H., Capece, V.R., King, A.J. and EL-Aini, Y.M., 1998, "Oscillating Cascade Aerodynamics at Large Mean Incidence," ASME Journal of Turbomachinery, Vol.120, No. 1, pp. 122-131 also ASME Paper No. 96-GT-339, 1996.

[11] Buffum, D.H., Capece, V.R., King, A.J. and EL-Aini, Y.M., 1996, "Experimental Investigation of Unsteady Flows at Large Incidence Angles in a Linear Oscillating Cascade," AIAA Paper No. 96-2823; also NASA TM-107283.

[12] Yoshihara, H. and Zonars, D., 1975, "The Transonic Jet Flap – A Review of Recent Results", Society of Automotive Engineers National Aerospace Engineering and Manufacturing Meeting, November 17-20, SAE Paper No. 751089.

[13] Seifert, A., Bachar, T., Koss, D., Shepshelovich, M. and Wygnanski, I., 1993, "Oscillatory Blowing: A Tool to Delay Boundary-Layer Separation," AIAA Journal, Vol. 31, No. 11, November.

[14] Seifert, A., Darabi, A. and Wygnanski, I., 1996, "Delay of Airfoil Stall by Periodic Excitation," Journal of Aircraft, Vol. 33, No. 4, July-August.

[15] Seifert, A. and Pack, L.G.., 1999, "Oscillatory Control of Separation at High Reynolds Numbers," AIAA Journal, Vol. 37, No. 9, September.

[16] Allan, B.G., Junag, J., Raney, D.L., Seifert, A., Pack, L.G. and Brown, D.E., 2000, "Closed-loop Separation Control Using Oscillatory Flow Excitation," NASA CR-2000-210325.

[17] Seifert, A. and Pack, L.G., 1999, "Active Control of Separated Flows on Generic Con□gurations at High Reynolds Numbers," AIAA Paper No. 99-3403.

[18] Kerrebrock, J.L., Reijnen, D.P., Ziminsky, W.S. and Smilg, L.M., 1997, "Aspirated Compressors," ASME Paper No. 97-GT-525.

[19] Kerrebrock, J.L., Drela, M., Merchant, A.A. and Schuler, B.J., 1998, "A Family of Designs for Aspirated Compressors," ASME Paper No. 98-GT-196.

[20] Lepicovsky, J., McFarland, E.R., Chima, R.V., and Wood, J.R., 2000, "On Flow□eld Periodicity in the NASA Transonic Flutter Cascade, Part I-Experimental Study", ASME Paper No. 2000-GT-0572, 2000: also, Lepicovsky, J., Chima, R.V., McFarland, E.R., and Wood, J.R., 2001, "On Flow□eld Periodicity in the NASA Transonic Flutter Cascade", Journal of Turbomachinery, Vol. 123, July, pp.501-509.

[21] Chima, R.V., McFarland, E.R., Wood, J.R. and Lepicovsky, J., 2000, "On Flow□eld Periodicity in the NASA Transonic Flutter Cascade, Part II-Numerical Study", ASME Paper No. 2000-GT-0573, 2000; also Lepicovsky, J., Chima, R.V., McFarland, E.R., and Wood, J.R., 2001, "On Flow□eld Periodicity in the NASA Transonic Flutter Cascade", Journal of Turbomachinery, Vol. 123, July, pp.501-509.

[22] Ayer, T.C. and Verdon, J.M., 1994, "Numerical Unsteady Aerodynamic Simulation for Blade Forced Response," Report WL-TR-95-2011.

[23] Carta, F.O., 1978, "Aeroelasticity and Unsteady aerodynamics," in The Aerothermodynamics of Aircraft Gas Turbine Engines, Editor Gordon C. Oates, AFAPL-TR-78-52.

[24] Chima, R.V., 1999, "TCGRID 3-D Generator for Turbomachinery, User's Manual and Documentation," NASA Glenn Research Center, December.

[25] Baldwin, B.S. and Lomax, H., 1978, "Thin Layer Approximation and Algebraic Model for Separated Turbulent Flows," AIAA Paper No. 78-257.

[26] Cebeci, T. and Smith, A.M.O., 1974, Analysis of Turbulent Boundary Layers, Academic Press, N.Y.

[27] Chima, R.V., Giel, P.W., and Boyle, R.J., 1993, "An Algebraic Turbulene Model For Three-Dimensional Viscous Flows," NASA-TM-105931, January.

[28] Bölcs, A. and Fransson, T.H., 1986, "Aeroelasticity in Turbomachines: Comparison of Theoretical and Experimental Cascade Results," Communication de Laboratoire de Thermique Appliquée et de Turbomachines, No. 1, Ecole Polytechnique Fédérale de Lausanne, Switzerland.

[29] Szechenyi, E. and Finas, R., 1981, "Aeroelastic Testing in a Straight Cascade Wind Tunnel," Aeroelasticity in Turbomachines, Edited by P. Suter, Juris-Verlag, pp. 143-149.

[30] Szechenyi, E. and Girault, J.Ph., 1981, "A Study of Compressor Blade Stall Flutter in a Straight Cascade Wind Tunnel," Aeroelasticity in Turbomachines, Edited by P. Suter, Juris-Verlag, pp. 163-169.

[31] Lepicovsky, J., McFarland, E.R., Capece, V.R., and Hayden, J., 2002, "Unsteady Pressures in a Transonic Fan Cascade due to a Single Oscillating Airfoil," ASME Paper No. GT-2002-30312.

[32] Hayden, J., Capece, V.R., and Lepicovsky, J., 2002, "The In□uence Coef-□cient Method for Airfoils Oscillating in Pitching Motion at Large Mean Incidence," AIAA Paper No. AIAA 2002-4087.

[33] Lepicovsky, J., Capece, V.R., and Ford, C.T., "Resonance Effects in the NASA Transonic Flutter Cascade Facility," ASME Paper No. GT-2003-38344, June 2003.

[34] Buffum, D.H. and Fleeter, S., 1990, "Aerodynamics of a Linear Oscillating Cascade," NASA Technical Memorandum 10350.

[35] Lepicovsky, J., McFarland, E.R., Capece, V.R., Jett, T.A., and Senyitko, R.G., 2002, "Methodology of Blade Unsteady Pressure Measurement in the NASA Transonic Flutter Cascade," NASA TM 2002-211894.

[36] Burgess, J., 1975, "On Digital Spectrum Analysis of Periodic Signals," Journal of the Acoustical Society of America, Vol. 58, No. 3, September, pp. 556-567.

[37] Gostelow, J.P., 1977, "A New Approach to the Experimental Study of Turbomachinery Flow Phenomena," ASME Journal of Engineering for Power, Vol. 99, pp. 97-105.

Additional References

[38] Bölcs, A., Fransson, T.H., and Schlä□i, D., 1989, "Aerodynamic Superposition Principle in Vibrating Turbine Cascades," AGARD, 74th Specialists' Meeting of the Propulsion and Energetics Panel on Unsteady Aerodynamic Phenomena in Turbomachines, Luxembourg, August 28 – September 1.

[39] Bölcs, A., Fransson, T.H., and Schlä□i, D., 1990, "Aerodynamic Superposition Principle in Vibrating Turbine Cascades," AGARD-CPP-468/469, pp. 5-1 – 5-19.

[40] Chen, J.P., Celestina, M., and Adamczyk, J.J., 1994, "A New Procedure for Simulating Unsteady Flows Through Turbomachinery Blade Passages," ASME Paper No. 94–GT-151.

[41] Buffum, D.H. and Fleeter, S., 1990, "Oscillating Cascade Aerodynamics by an Experimental In□uence Coefficient Technique," AIAA Journal of Propulsion and Power, Vol. 6, No. 5, pp. 612-620.

[42] Bölcs, A., Fransson, T.H., and Schlä□i, D., 1989, "Aerodynamic Superposition Principle in Vibrating Turbine Cascades," AGARD, 74th Specialists' Meeting of the Propulsion and Energetics Panel on Unsteady Aerodynamic Phenomena in Turbomachines, Luxembourg, August 28 – September 1.

[43] Fransson, T.H., 1990, "Analysis of Experimental Time-Dependent Blade Surface Pressures from an Oscillating Turbine Cascade with the In□uence-Coefficient Technique," ASME Paper No. 90-GT-225.

[44] Boldman, D.R. and Buggele, A.E., 1978, "Wind Tunnel Tests of a Blade Subjected to Midchord Torsional Oscillations at High Subsonic Stall Flutter Conditions", NASA TM-78998.

[45] Shaw, L.M., Boldman, D.R., Buggele, A.E., and Buffum, D.H., 1986, "Unsteady Pressure Measurements on a Biconvex Airfoil in a Transonic Oscillating Cascade", Journal of Engineering for Gas Turbines and Power, Vol. 108, pp. 53-59.

[46] Capece, V.R. and Fleeter, S., 1987, "Forced Response Unsteady Aerodynamics in a Multistage Compressor," Report No. ME-TSPC-TR-87-12.

[47] Lepicovsky, J., Chima, R.V., Jett, T.A., Bencic, T.J., and Weiland, K.E., 2000, "Investigation of Flow Separation in a Transonic-Fan Cascade Using Visualization Methods", NASA/TM-2000-210521, Dec.

[48] Capece, V.R. and Fleeter, S., 1989, "Measurement and Analysis of Unsteady Flow Structures in Rotor Blade Wakes," Experiments in Fluids, pp. 61-67.

[49] Ekaterinaris, J.A. and Platzer, M.F., 1997, "Computational Prediction of Airfoil Dynamic Stall," Progress in Aerospace Sciences, Vol. 33, No. 11/12, pp. 759-846.

[50] Gerolymos, G.A., 1990, "Periodicity, Superposition, and 3D Effects in Supersonic Compressor Flutter Aerodynamics," International Journal of Turbo and Jet Engines, Vol. 7, pp. 143-152.

[51] Hassan, A. and JanakiRam, R.D., 1997, "Effects of Zero-Mass 'Synthetic' Jets On The Aerodynamics Of The NACA-0012 Airfoil," AIAA Paper No. 97-2326.

[52] Lepicovsky, J., McFarland, E.R., and Capece, V.R., "Unsteady Airfoil Pressure Measurements in the NASA Transonic Flutter Cascade," Sixth National Turbine Engine High Cycle Fatigue Conference, March 2001.

[53] Lord, W.K., MacMartin, D.G. and Tillman, T.G., 2000, "Flow Control Opportunities in Gas Turbine Engines," AIAA Paper No. 2000-2234.

[54] Ravindran, S.S., 1999, "Active Control of Flow Separation Over an Airfoil," NASA TM-1999-209838.

[55] Smith, S.N., 1973, "Discrete Frequency Sound Generation in Axial Flow Turbomachines," Aeronautical Research Council Reports and Memoranda No. 3709.

[56] Smith, B.L. and Glezer, A., 1997, "Vectoring and Small-Scale Motions Effected in Free Shear Flows Using Synthetic Jet Actuators," AIAA Paper No. 97-0213.

[57] van Dyken, R.D., Ekaterinaris, J.A., Chandrasekhara, M.S. and Platzer, M.F., 1996, "Analysis of Compressible Light Dynamic Stall Flow at Transitional Reynolds Numbers," AIAA, Vol. 34, pp. 1420-1427.